Physics – Uspekhi **41** (1) 49 – 76 (1998)

REVIEWS OF TOPICAL PROBLEMS PACS numbers: **61.46.+w**, **85.42.+m**

Effects of the nanocrystalline state in solids

A I Gusev

Contents

Abstract. Recent results on the effect of the nanocrystalline state on the mechanical, thermal, and magnetic properties and microscopic structure of metals and solid-phase compounds are reviewed. Basic methods for preparing compact nanocrystalline materials are briefly discussed. Size effects in such materials are discussed in detail and the importance of interfaces in determining the structure and properties of compact nanomaterials is demonstrated. Models explaining the structural features and anomalous properties of nanocrystalline solids are analyzed.

1. Introduction

The problem of fabricating finely dispersed powders of metals, alloys, and compounds and ultrafine-grained materials manufactured from them for various areas of technology has been discussed for a long time in the literature. In the last decade there has been an upsurge of interest in this area of research, since it was found (primarily in metals) that when the crystallite size becomes smaller than a certain threshold value, the properties of such substances change considerably [1 – 14]. These effects can be observed when the average size of the crystalline grains does not exceed 100 nm and manifest themselves most vividly for grain sizes smaller than 10 nm. The study of the properties of ultrafine-grained materials requires consideration not only of their composition and structure but also of the degree of dispersion. Polycrystalline ultrafine-grained materials with an average grain size ranging from 100 – 150 down to 40 nm are usually called submicrocrystalline (SMC) materials and those with an average grain size below 40 nm, nanocrystalline (nc) materials.

The fact that the properties of small particles differ from those of bulk material has been known for a long time and used in different fields of technology. Examples are the highly effective catalysts fabricated from finely dispersed powders or ceramics with nanometer grains; radio-wave absorbing ceramic materials (used in aviation), whose matrix contains finely dispersed metallic particles distributed at random; and widely used aerosols. Suspensions of metallic nanoparticles (usually iron or its alloys) with sizes ranging from 30 nm down to 1 – 2 μm are used as additions to motor oils to regenerate the worn-out parts of automobile and other engines directly during operation. Nanoparticles are widely used in manufacturing microelectronic devices. In x-ray and UV optics, special mirrors with multilayer coatings of alternating thin layers of elements with high and low densities are employed (e.g., tungsten and carbon or molybdenum and carbon); a pair of such layers is about 1 nm thick, with the layers being smooth at the atomic level. Other optical devices with nanosize elements, intended for use primarily in x-ray microscopy, are Fresnel zone plates with the smallest zone width near 100 nm and diffraction gratings with spacings smaller than 100 nm.

The blades of gas turbines of turbojet engines are devices that operate under the most extreme conditions. The changeover to a new generation of gas-turbine engines requires structural materials that have 20% higher strength and hardness, 50% greater fracture toughness, and more than double wear resistance. Field tests have shown that the use of nanocrystalline high-temperature alloys in gas turbines ensures at least half of the required increases in the above characteristics. Ceramic nanomaterials are widely used in the manufacture of parts operating at extreme temperatures, under inhomogeneous thermal stresses, and in aggressive media. The superplasticity of ceramic nanomaterials allows them to be employed for manufacturing parts of complex configurations with highly accurate

A I Gusev Institute of Solid-State Chemistry Ural Branch
of the Russian Academy of Sciences
Pervomaiskaya ul. 91, 620219 Ekaterinburg, Russia
Tel. (7-3432) 49-3523. Fax (7-3432) 44-4495
E-mail: gusev@chem.ural.ru

Received 10 September 1997
Uspekhi Fizicheskikh Nauk **168** (1) 55 – 83 (1998)
Translated by Eugene Yankovsky; edited by S N Gorin

dimensions for aerospace engineering. Also, due to their biocompatibility and high strength, hydroxylapatite-based nanoceramic materials are used in orthopedics for fabricating artificial joints and in dentistry. Nanocrystalline ferromagnetic alloys of Fe–Cu–*M*–Si–B systems (*M* stands for a transition metal of Groups IV–VI) find application as perfect transformer magnetically soft materials with an extremely low coercive force and a high magnetic permeability.

The small size of the grains guarantees that the grain boundaries are well-developed and long. If we employ an approximation in which the grains are balls of diameter d and the interface (grain boundary) has a thickness δ, then the fraction of grain boundaries in the overall volume of a particle is

$$\frac{\Delta V}{V} = \left[\frac{\pi}{6}\,d^3 - \frac{\pi}{6}(d-2\delta)^3\right]\left(\frac{\pi}{6}d^3\right)^{-1} \approx \frac{6\delta}{d}\,.$$

If the grain boundary is 3 to 4 atomic layers (0.5–1.5 nm) and the grain size is 10 to 20 nm, almost 50% of all the substance is involved in the interfaces. In nanomaterials with grain sizes ranging from 100 down to 10 nm, the interfaces contain 10 to 50% of all atoms of the nanocrystalline solid. Moreover, the grains themselves have various atomic defects, e.g., vacancies or complexes of them and disclinations and dislocations, whose number and distribution differ considerably from those in big grains, which are 5 to 100 μm in size or larger. Because of these features of the structure of nanocrystalline materials, the properties of such materials differ from those of ordinary polycrystals. For this reason, at present decreasing the grain size is considered an effective method of changing the properties of solids.

Indeed, there are indications that the nanocrystalline state affects the properties of ferromagnets (the Curie point, coercive force, and saturation magnetization) and the magnetic susceptibility of weak (para and dia) magnets; that memory effects emerge in the elastic properties of metals, and their heat capacity and hardness change markedly; that in semiconductors, optical and luminescent properties alter; and that plasticity becomes a characteristic feature of boride, carbide, nitride, and oxide materials, which in the ordinary coarse-grained state are brittle. Nanocrystalline materials have an exceptionally high diffusion mobility of atoms (exceeding the diffusion mobility in ordinary polycrystals by a factor of 10^5–10^6), but the mechanisms of diffusion processes in nanocrystalline substances have yet to be understood and the literature contains contradictory explanations of such behavior. What remains unclear is the microstructure of nanocrystals, i.e., the structure of the grain boundaries and their atomic density and the effect of nanopores and other free volumes on the properties of nanocrystals.

Usually, when dealing with a nonequilibrium metastable state, it is assumed that there exists a real equilibrium state associated with a given metastable state. For example, a metastable glassy (amorphous) state can be associated with an equilibrium liquid state (a melt). What sets the nanocrystalline state apart from other known nonequilibrium metastable states of matter is the absence of any equilibrium state corresponding to the nonequilibrium, with similar structure and development of grain boundaries.

Nanocrystalline materials represent a special state of condensed matter: macroscopic ensembles of extremely small particles with sizes of several nanometers. The unusual properties of these materials are due to both the features of individual grains (crystallites) and the collective behavior of the grains, which depends on the nature of the interaction between nanoparticles.

The main objective of this work is to discuss the effects of the nanocrystalline state observed in the structure and properties of compact metals and compounds. In this paper we do not examine the features of structure and properties of isolated nanoparticles (clusters) and nanopowders, since all of these aspects have been thoroughly discussed and generalized in the literature [1–11, 14–21]. The overwhelming majority of studies of compact nanocrystalline materials incorporate both scientific and technological aspects. The next problem is related to the microstructure of compact nanomaterials and its stability, the state of grain boundaries and their relaxation; and the direct study of the microstructure by various electron-microscopic, diffraction, and spectroscopic methods. Closely linked to this area of research is the investigation of the structure of compact nanomaterials by indirect methods (the study of phonon spectra, calorimetry, and measurements of elastic properties yield information about the thermodynamic characteristics of the nanocrystalline state and the degree of its deviation from a thermodynamically equilibrium coarse-grained polycrystalline state; research into the temperature dependence of microhardness, elastic moduli, and electron transport properties is used to study the growth of grains and relaxation of the grain boundaries). Since it is assumed that compact nanomaterials will find broadest application as structural materials in high-tech areas (due to the unique combination of their mechanical properties) and as magnetic materials (primarily, nanocrystalline low-coercivity alloys), we can clearly identify two more areas of research, i.e., the study of mechanical and magnetic properties. The effect of the nanocrystalline state of the electronic structure of compact materials has been studied very poorly and been almost entirely ignored in the literature, although there has been intensive research of the electronic structure of nanoclusters and isolated nanoparticles.

The structure and size dispersion and hence the properties of nanocrystalline materials depend on the method by which the materials are produced, so that in the first part of this review we briefly discuss the main methods of preparing compact nanocrystalline materials.

2. Preparation of compact nanocrystalline materials

2.1 Compacting powders

The methods of preparing isolated nanocrystalline particles, nanoclusters, and nanopowders are extremely diversified and have been thoroughly developed (this is especially true of the best-known methods, such as gas-phase evaporation and condensation, deposition from colloidal solutions, plasma-chemical synthesis, and various types of thermal decomposition). Compact nanocrystalline materials have been produced only in the last years: the pioneering work in compacting nanopowders was done between 1981 and 1986 [22–24]. At present, compacting nanopowders is one of the most widespread methods of preparing compact nanomaterials.

The huge fundamental interest in compact nanocrystalline materials is primarily due to there being very convenient objects for observation. This was the reason for the wide popularity of the method of preparing nanocrystalline

materials proposed in Refs [22–26] (Fig. 1). The approach described in these papers uses the method of evaporation and condensation for preparing nanocrystalline particles that are deposited on the cold surface of a cylinder rotating in an atmosphere of a rarefied inert gas, usually helium; if helium is replaced by xenon (at the same pressure), which is a denser gas, the particle size grows several-fold. The particles of the condensate are usually faceted. Under the same conditions of evaporation and condensation, metals with a higher melting point produce smaller particles. The condensate is scraped off by a special device from the cylinder's surface and gathered into a collector. After the inert gas has been evacuated from the chamber, a preliminary (at a pressure of 1 GPa) and final (at a pressure of up to 10 GPa) pressing of nanocrystalline powder are carried out. As a result one gets cylinder plates with diameters ranging from 5 to 15 mm, thicknesses ranging from 0.2 to 3.0 mm, and densities up to 70 to 90% of the theoretical value of the corresponding material (up to 97% for nanocrystalline metals and up to 85% for ceramic nanomaterials [6]). Depending on the conditions of evaporation and condensation, compact nanocrystalline materials produced by this method consist of particles with an average size d ranging from 1–2 nm to 80–100 nm. The particle-size distribution is lognormal and is described by the function

$$F(d) = \left(\sqrt{2\pi}\ln\sigma_g\right)^{-1}\exp\left[-\frac{(\ln d - \ln d_g)^2}{2\ln^2\sigma_g}\right], \qquad (1)$$

where d is the particle diameter, d_g the geometrical-mean diameter, and σ_g the variance

$$\ln\sigma_g = \left[\frac{\sum n_i(\ln d_i - \ln d_g)^2}{\sum n_i}\right]^{1/2}.$$

Analysis shows that most distributions of metal nanoparticles produced by the evaporation–condensation method are described by formula (1) with $\sigma_g = 1.4 \pm 0.2$.

Since there is no contact with the surroundings in the process of nanopowder production and pressing, contamination of the compact nanocrystalline samples is avoided, which is extremely important for studies of the nanocrystalline state of metals and alloys. The apparatus described in [22–26] can also be used for the production of nanocrystalline compounds such as oxides and nitrides. In this case the metal is evaporated into an oxygen- or nitrogen-containing atmosphere.

The porosity of ceramic nanomaterials produced by compacting powders is due to triple junctions of crystallites. A decrease in powder size is accompanied by a substantial decrease in powder compactibility upon pressing at the same pressure [27]. A decrease in porosity and a more uniform distribution of porosity are achieved by compacting at an elevated temperature such that no intense recrystallization has yet been observed. For instance, ordinary sintering of a fine powder of zirconium oxide consisting of particles 40–60 nm in diameter at 1370 K for 10 s makes it possible to achieve a relative density of 72% with an average grain size of 120 nm in the sintered sample; hot pressing at the same temperature and a pressure of 1 GPa makes it possible to produce a sintered material with a relative density of 87% and an average grain size of 130 nm [28]. Lowering the sintering temperature to 1320 K and increasing the sintering period to 5 h makes it possible to prepare compacted zirconium oxide (ZrO_2) with a relative density exceeding 99% and an average grain size of 85 nm [29]. Andrievski et al. [30] produced compacted samples with a density of 98% of the theoretical value by hot pressing of a titanium nitride powder ($d \approx 80$ nm) at 1470 K at a pressure of 4 GPa, but (according to diffraction data) because of the intense recrystallization that followed hot pressing, the average grain size was no smaller than 0.3 μm. Rabe and Wäsche [31] found that the densest (with a relative density of 98%) samples of titanium nitride are prepared by sintering samples compacted from the finest nanopowders ($d \approx 8$–25 nm) with minimum variance of grain size.

On the whole, compaction followed by high-temperature sintering of nanopowders is an extremely promising method for preparing compact nanocrystalline materials, especially ceramic materials. In implementing this method one should avoid grain coarsening at the stage of sintering of compacted samples. This is possible at high compact densities (no less than 0.7 of the x-ray density), when sintering is relatively rapid and the temperature is relatively low, $T \leqslant 0.5T_m$ (T_m is the melting point). Achieving such high compact densities is a serious problem, since nanocrystalline powders have a reduced compactibility and ordinary methods of static pressing do not result in a high enough density. The physical

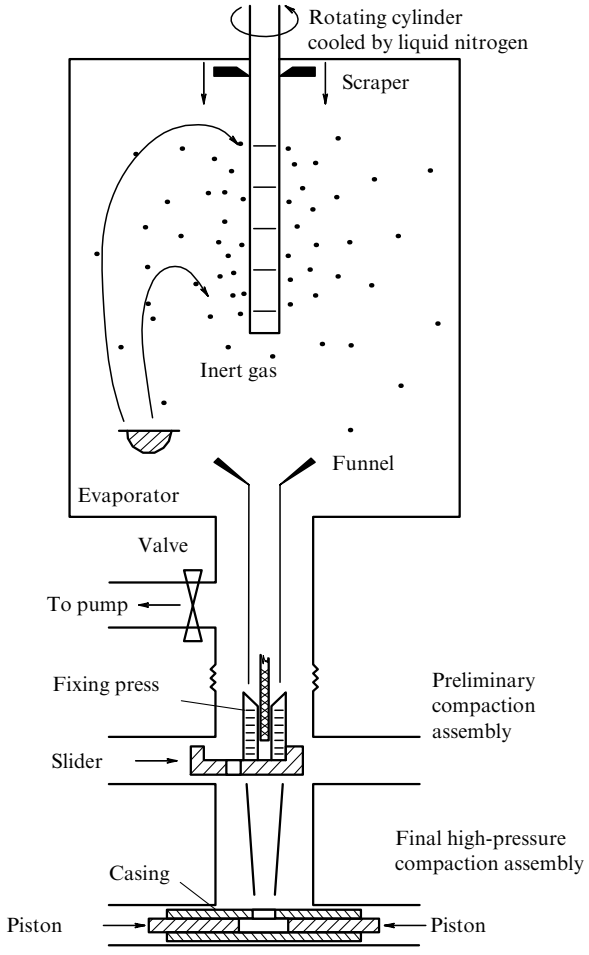

Figure 1. Schematic of the chamber for preparing compact nanocrystalline materials: a substance evaporated or sputtered from one or several sources condenses in the atmosphere of a rarefied inert gas and is deposited on the cold surface of a rotating cylinder; the condensate is scraped off, collected, and pressed in a vacuum (after the inert gas has been pumped out).

reason for the low compactibility of nanopowders lies in the interparticle adhesion forces, which increase sharply as the particles get smaller.

An effective way of keeping the grains in compacted nanomaterials small is (in addition to lowering the sintering temperature) to add alloying components that hinder rapid grain growth. The production of nanocrystalline hard alloys WC – Co may serve as an example [32 – 36]. A nanocrystalline powder composite of tungsten carbide and cobalt was produced by thermal decomposition of organometallic precursors with subsequent carbothermic reduction in the fluidized bed, so that the layer retained its high dispersity. To hinder grain growth and reduce the solubility of tungsten carbide in cobalt, up to 1 wt.% nonstoichiometric vanadium carbide was added to the mixture. The hard alloy produced from this nanocrystalline composite has an optimum combination of extreme hardness and high strength [33 – 35]. Seegopaul et al. [36] found that each nanocomposite WC – Co particle, which is roughly 75 μm in diameter, consists of several million nanocrystalline WC grains, each smaller than 50 nm, distributed within the cobalt matrix. Sintering the nanocomposite mixture of tungsten carbide with 6.8 wt.% Co and 1 wt.% VC produced alloys in which 60% of WC grains were smaller than 250 nm and 20% smaller than 170 nm. An alloy containing, in addition to tungsten carbide, 9.4 wt.% Co, 0.8 wt.% Cr_3C_2, and 0.4 wt.% VC was found to have finer grains. Even after sintering at the relatively high temperature of 1670 K, 60% of the tungsten carbide grains in this alloy were smaller than 140 nm and 20% smaller than 80 nm. Comparison of the nanocrystalline alloy and the ordinary polycrystalline alloy demonstrated that the nanoalloy was considerably stronger and much more tough.

An effective way to compact nanocrystalline powders is to employ the pulsed magnetic compression method suggested by Ivanov et al. [37, 38]. In contrast to stationary compacting methods, the propagation of pulsed compression waves is accompanied by intense heating of the powder due to rapid release of energy of friction between particles in the packing process. If the particles are relatively small, $d \leqslant 0.3$ μm, the time it takes the particles to get heated by heat diffusion from the surface proves to be much shorter than the characteristic duration of the pulsed compression waves (1 – 10 μs). Due to high surface energy of the powder, dynamic hot compaction of an ultra-disperse powder can be achieved under certain conditions by selecting the proper values of the parameters of the compression wave. The pulsed magnetic compression method enables generating pulsed compression waves with amplitudes up to 5 GPa and pulse lengths of several microseconds. The method is based on the idea of concentration of the action of the magnetic fields of high-power pulsed currents, makes it possible to effectively control the parameters of the compression wave, is ecologically clean, and is much safer than the dynamic methods that use explosives. Aluminum nitride (AlN) powders produced by the electric explosion technique were compacted using pulsed magnetic compression at a pressure up to 2 GPa to a density of 95% of the theoretical values, while with Al_2O_3 the density reached was as high as 86%. The pulsed magnetic compression method has been used to fabricate products of various shapes, and in most cases these products require no further machining. In particular, fabrication of superconducting oxide ceramic materials using the pulsed magnetic compression method was achieved by Ivanov et al. [38]. The samples had a density higher than 95% of the theoretical value.

By employing pulsed pressure, one can reach higher compaction densities in comparison to the results achieved by static pressing. This suggests that when the powder medium is in a state of rapid movement, the interparticulate forces are effectively overcome.

The pulsed magnetic compression method was used to compact nanocrystalline powders of Al_2O_3 [39, 40] and TiN [41]. The results of Andrievskii et al. [41] show that raising the compaction temperature to roughly 900 K is much more effective than increasing pressure in cold pressing. The compacts of nanocrystalline TiN produced at a pulsed pressure of 4.1 GPa and a temperature of 870 K were found to have grains of roughly 80 nm in diameter and a density of 83% of the theoretical value. Lowering the compaction temperature to 720 K was accompanied by a lowering in density to 81%.

2.2 Deposition on a substrate

Deposition on a cold or heated substrate is a method by which films and coatings are manufactured, i.e., continuous layers of nanocrystalline materials. Here, in contrast to gas-phase synthesis, nanoparticles form directly on the surface of the substrate rather than in the volume of the inert gas near the cooled wall. Pressing is not needed in this case since the resulting nanocrystalline material has already been compact.

Deposition onto a substrate may occur from vapor, plasma, or a colloidal solution. In the case of deposition from a vapor, the metal is evaporated in vacuum, oxygen or a nitrogen-containing atmosphere, and the vapor of the metal or a compound (oxide or nitride) condenses on the substrate. The size of the crystallites in the film can be controlled by varying the evaporation rate and the substrate temperature. Most often this method is used to produce nanocrystalline metal films [42, 43]. A film of zirconium oxide alloyed with yttrium oxide, with an average crystallite size of 10 to 30 nm, was produced by pulsed laser evaporation of metals in a beam of oxygen ions and subsequent deposition of the resulting oxides on the substrate with a temperature of 350 to 700 K [44].

When the deposition is made from a plasma, an inert gas is used to maintain the electric discharge. The film's continuity and thickness and the crystallite size can be controlled by changing the gas pressure and the discharge parameters. A source of metallic ions in deposition from a plasma is usually a metal cathode. Such cathodes guarantee a high degree of ionization (from 30 to 100%); the kinetic energy of ions ranges from 10 to 200 eV, and the deposition rate can reach values close to 3 μm/min. By exposing chromium to the plasma of an arc discharge in a low-pressure argon atmosphere, Dudko et al [45] and Barg et al. [46] produced a chromium film on a copper substrate, with a crystallite size of roughly 20 nm; films thinner than 500 nm were found to have an amorphous structure, while those thicker than 500 nm were crystalline. The extreme hardness (up to 20 GPa) of the films was due to the formation of ultra supersaturated solid solutions of interstitial impurities (C and N) in chromium.

Ion-plasma coatings consisting of titanium nitride and titanium carbonitride have found wide application. Heating the substrate to 500 – 800 K makes it possible to retain the nanocrystalline structure of the coating. The various methods of preparing coatings and films of high-melting compounds and the properties of such coatings and films have been discussed in detail in Andrievskii's review [47].

Usually, with deposition from a plasma, reactive media (argon–nitrogen and argon-hydrocarbon mixtures at a pressure of roughly 0.1 Pa) and metal cathodes are employed. The main drawbacks of ion-plasma arc sputtering are the formation of fine metal drops caused by partial melting of the cathode and the possibility of these droplets landing on the deposited films.

A variant of plasma deposition is magnetron sputtering, which makes it possible to use cathodes made not only from metals and alloys but also from various compounds and to lower the substrate temperature to 100 – 200 K or even lower. This broadens the possibility of fabricating amorphous and nanocrystalline films. However, the degree of ionization, the ion kinetic energy, and the deposition rate in magnetron sputtering are lower than in the arc-plasma method.

Van Swygenhoven et al. [48] used magnetron sputtering of a $Ni_{0.75}Al_{0.25}$ target and deposition of metallic vapors on an amorphous substrate to fabricate intermetallic films of Ni_3Al with an average crystallite size of about 20 nm.

Oxide semiconducting films are produced by deposition on a substrate from colloidal solutions. The method consists of the following stages: preparation of the solution, deposition on the substrate, drying, and annealing. Deposition of oxide nanoparticles has produced semiconducting films of ZnO, SnO_2, TiO_2, and WO_3 [49 – 53]. Nanostructured films containing nanoparticles of different semiconductors can be produced by the coprecipitation method. Yamada et al. [54] describe the production of nanocrystalline films of ZrO_2.

The common methods of film deposition are chemical or physical vapor deposition from the gas phase (CVD and PVD). These methods have long been used to fabricate films and coatings for various purposes. Usually the crystallites in such films are large, but in multilayer and multiphase CVD films, nanostructures can also be produced [14, 47]. Deposition from the gas phase is usually related to high-temperature gas reactions of metal chlorides in a hydrogen – nitrogen or hydrogen – hydrocarbon atmosphere. The temperature range in which CVD films are deposited is 1200 – 1400 K, and the deposition rate is 0.03 – 0.2 μm min^{-1}. The use of laser light makes it possible to reduce the temperature in the deposition process to 600 – 900 K, which facilitates the formation of nanocrystalline films.

In recent years, organometallic precursors of the tetraethane(ethyl)amide type, $M[N(CH_3)_2]_4$ and $M[N(C_2H_5)_2]_4$, which are characterized by a high vapor pressure, have been used in the deposition from the gas phase. In this case the decomposition of the precursor and the activation of reagent gas (N_2 and NH_3) are done via electron cyclotron resonance.

A characteristic feature of transition-metal nitride films produced by various deposition methods is the hyperstoichiometric nitrogen content (in comparison to the $MN_{1.0}$ phases with the base structure *B*1 (NaCl)), e.g., Zr_3N_4, Hf_3N_4, Nb_4N_5, Ta_3N_5, etc.

2.3 Crystallization of amorphous alloys

In this method the nanocrystalline structure is created in an amorphous alloy via crystallization of the latter. The melt spinning method, i.e., the fabrication of thin ribbons of amorphous metal alloys via rapid (at a rate of $\geqslant 10^6$ K s^{-1}) cooling of the melt on the surface of a rotating disk or drum, has been thoroughly developed. The amorphous ribbon is then annealed at a carefully controlled temperature for its crystallization. To produce a nanocrystalline structure, the annealing is done in such a way that a large number of crystallization centers appear but the crystal growth rate is low. In the first stage of crystallization, small crystals of intermediate metastable phases may appear. For instance, Lu et al. [55] studied a Ni-based amorphous alloy and found that small crystals of a highly supersaturated metastable solid solution of phosphorus in nickel Ni(P) are the first to form and that this process is followed by the emergence of nickel phosphide crystals. It is assumed that the barrier for crystal growth is the amorphous phase.

A nanocrystalline ribbon can also be obtained directly in the spinning process. Cheng [56] employed this method to produce strips of the $Ni_{65}Al_{35}$ alloy. The strip consisted of crystals of the intermetallic compound NiAl with an average grain size of ~ 2 μm; the crystals have an extremely uniform microtwin substructure with a characteristic size of several tens of nanometers. Such a structure impeded the development of microcracks, and hence raised the ductility and toughness of the brittle intermetallic compound NiAl.

The crystallization of amorphous alloys is under intensive study in connection with the possibility of producing nanocrystalline ferromagnetic alloys of Fe – Cu – *M* – Si – B systems (where *M* is Nb, Ta, W, Mo, or Zr), which have an extremely weak coercive force and high magnetic permeability, i.e., soft-magnetic materials.

Hoffmann [57] studied thin films of the Ni – Fe alloy and found that the soft-magnetic properties of these films improve as the effective magnetocrystalline anisotropy reduces. This can be attained by increasing the number of grains participating in the exchange interaction in thin magnetic films. In other words, a decrease in size leads to an increase in the strength of the exchange interaction and a reduction in the magnetocrystalline anisotropy and hence to an improvement of the soft-magnetic properties. Later this idea was realized in the directional crystallization of multicomponent amorphous alloys.

Silicon-containing steels are soft-magnetic materials, so that the first attempts in improving the soft-magnetic properties via crystallization of amorphous alloys involved Fe – Si – B systems with copper additives. But all attempts to produce alloys with a nanocrystalline structure in this system failed. Only when transition metals of the Groups IV – VII were introduced into the amorphous alloy Fe – Si – B as additives (in addition to copper) did a nanocrystalline structure form as a result of crystallization [58]. The crystallization of amorphous alloys of the Fe – Cu – Nb – Si – B type at 700 – 900 K produced an alloy with a uniform nanocrystalline structure. In this alloy, grains of the bcc α-Fe(Si) phase roughly 10 nm in diameter and copper clusters smaller than 1 nm are uniformly distributed in the amorphous matrix. Preliminary (prior to crystallization annealing) deformation by rolling amorphous Fe – Cu – M – Si – B alloys or low-temperature annealing reduces the grain size to ~ 5 nm [59, 60].

As a result of crystallization of rapidly solidified amorphous Al – Cr – Ce – *M* aluminum alloys (here *M* is Fe, Co, Ni, or Cu) with 92 at.% Al, a structure emerges that contains an amorphous phase and aluminum-rich icosahedral quasicrystalline nanoparticles that precipitate in the amorphous phase (Fig. 2) [61]. These alloys have extremely high tensile strengths (up to 1340 MPa) close to, or even exceeding, the value for steels. The main reasons for this are the spherical morphology of icosahedral nanoparticles and the presence of a thin layer of aluminum surrounding these particles.

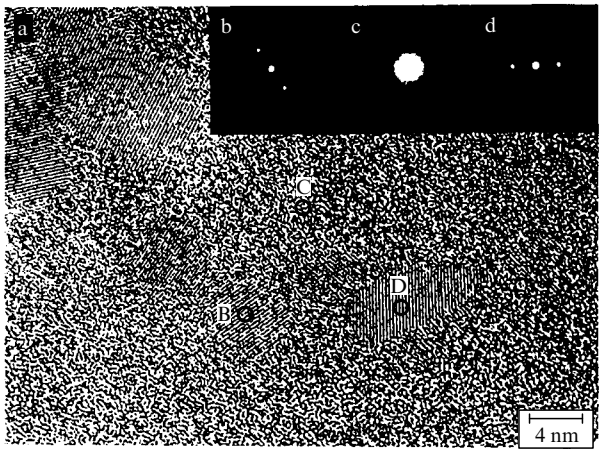

Figure 2. (a) Microphotograph of the rapidly solidified alloy $Al_{94.5}Cr_3Ce_1Co_{1.5}$ [61]: icosahedral nanoparticles B, D, etc. with an average diameter of 5 – 10 nm distributed in C (the amorphous matrix); b, c, and d are diffraction patterns taken from areas 1 nm in diameter indicated by circles and belonging to the regions B, C, and D, respectively.

At present the production of nanocrystalline alloys by crystallizing a quenched amorphous state is being actively developed and the number of alloys with a nanocrystalline structure obtained by this method is growing fast.

2.4 Intense plastic deformation

A promising way of producing compact materials with extremely small grains ($\leqslant 100$ nm), or submicrocrystalline (SMC) materials, is to employ intense plastic deformation [62 – 65]. This method of fabricating SMC materials is based on the formation, as a result of large deformations, of a highly fragmented and disordered structure that nevertheless shows signs of a remanent recrystallized amorphous state. Various methods are used to attain high strains in the material: torsion under quasihydrostatic pressure, equichannel corner extrusion, rolling, and isotropic forging. The idea of these methods consists in generating multiple intense plastic shear deformations in the processed materials; here true strains $e = 4 - 7$ are reached. In addition to reducing the average grain size, the method makes it possible to fabricate massive samples of materials with a structure that is practically nonporous, which cannot be achieved by the method of compacting fine-grain powders.

In their reviews, Valiev et al. [65, 66] analyze the results of studies of the structure and properties of SMC materials.

A distinctive feature of SMC materials produced by deformation methods is the presence of nonequilibrium grain boundaries, which act as a source of large elastic stresses. Another source of stresses are triple grain junctions. An indication that the boundaries are nonequilibrium is the diffuse contrast of the boundaries and the bend extinction contours in grains observed in electron-micrographs of such materials. According to various estimates, the width of grain boundaries in SMC materials ranges from 2 to 10 nm. The nonequilibrium grain boundaries contain a large number of dislocations, and there are uncompensated disclinations at grain junctions. The density of dislocations in SMC materials produced by intense plastic deformation amounts to $\sim 3 \times 10^{15}$ m^{-2}, and the disclination strength is $1 - 2^\circ$. Note that the dislocation density inside grains is much smaller than at the boundaries. The dislocations and disclinations generate long-range stress fields concentrated near grain boundaries and triple junctions and are the main source of excess energy of grain boundaries. For instance, for SMC copper with an average grain size of roughly 200 nm the excess grain-boundary energy reaches 0.5 J m^{-2}. Annealing of the deformed material leads to a relaxation of the stresses and an equilibrium state of the grain boundaries.

The method of intense plastic deformation has been employed in the production of submicrograined structures of metals such as copper [67 – 69], palladium [70 – 73], iron [74 – 76], nickel [67, 69, 77 – 79], cobalt [80], and aluminum-based [64], magnesium-based [81], and titanium-based [82, 83] alloys.

Cziraki et al. [69] noted the difference in the microstructure of Ni and Cu produced by equal plastic deformations: in nickel SMC materials the majority of grains were about 100 nm in diameter, while in copper SMC materials the grain size varied from 5 to 100 nm, with copper grains having more defects (dislocations and twins) than nickel grains. This means than in nickel SMC materials the redistribution of dislocations into configurations that are energy-preferable (dislocations walls) already occurs during intense plastic deformation, while in SMC copper material such redistribution does not even begin. The results of Cziraki et al. [69] indicate that the microstructure of various materials produced by intense plastic deformation differs considerably at the various stages of deformation; moreover, it strongly depends on the deformation mode (pressure, shear, or torsion) and its parameters (the temperature, the amount, the rate, and the duration of deformation).

Indeed, to understand the structure and properties of SMC materials, it is highly important to take into account phase and structural transformations that occur in these materials upon heating or cooling, primarily such transformations as recrystallization, dissolution and precipitation of the second phase. The threshold temperature of stability of an SMC structure depends on the state of grain boundaries, which, in turn, depends on the conditions under which the structure was produced. The composition of the alloy and type of crystal lattice also have an appreciable effect on the structure of SMC materials and their recrystallization, but to our knowledge, these aspects have been ignored in the literature almost entirely.

The method of intense plastic deformations has been used to produce SMC structures not only in ductile metals, alloys, and intermetallic compounds but also in several highly brittle compounds. Interestingly, after plastic deformation to the same amount, the grains in brittle compounds were smaller than in metals. For instance, Rempel' et al. [84, 85] applied torsion under quasihydrostatic pressure to a coarse-grained ($D \approx 2 - 5$ μm) powder of nonstoichiometric titanium carbide $TiC_{0.62}$ and were the first to produce a compact nanocrystalline sample with grains 30 to 40 nm in diameter.

The formation of an SMC structure by deformation methods is accompanied by appreciable changes in the physical properties of metals, alloys, and compounds. Metals with an SMC structure serve as convenient models for experimental studies of the intercrystallite boundaries, since well-known methods of metal and solid-state physics can be employed [74, 75] in this case.

3. Microstructure of compact nanomaterials

The difference in the properties of nanocrystalline and coarse-grained materials is due to the different size of the crystallites and the highly developed interfaces, which contain up to 50% of all atoms of a nanocrystal. At present many scientists involved in studies of nanocrystalline materials believe that the special features (especially the mechanical ones) of such materials can be explained precisely by the length and structure of the interfaces. For this reason, most studies of the microstructure of compacted nanocrystalline materials focus on the features of the grain boundaries.

3.1 Grain boundaries in compacted nanomaterials

The density of the nanocrystalline materials prepared by different methods of compacting nanopowders [22–26, 28, 29, 37–39] is from 79–80% to 95–97% of the theoretical value. In the simplest case, the nanocrystalline material consisting of atoms of a single species contains two components that differ in structure [86]: ordered grains (crystallites) 5–20 nm in diameter, and intercrystallite boundaries up to 1.0 nm wide (Fig. 3). All the crystallites have the same structure and differ only in crystallographic orientation and size. The structure of the interfaces is determined by the type of interatomic interaction (metallic, covalent, ionic) and the mutual orientation of neighboring crystallites. The different orientation of neighboring crystallites somewhat reduces the density of matter in the interfaces. Moreover, the atoms belonging to the interfaces have nearest neighborhood that differs from that of atoms in the crystallites. Indeed, x-ray and neutron-diffraction studies of nanocrystalline compacted palladium (nc-Pd) [1, 87] have revealed that the density in the interfacial regions is 20 to 40% lower than that of ordinary palladium, and the coordination number of an atom belonging to an interface is smaller than that of an atom in an ordinary crystallite. The width of interfaces determined by different methods for different compacted nanocrystalline materials amounts to 0.4 to 1.0 nm [88–91].

According to the first models [2, 26, 92], the structure of the interfacial component is characterized by a random distribution of atoms and the absence not only of long-range but also of short-range order. The authors of [2, 26, 92] called this a gaslike structure, having in mind not the mobility of the atoms but their mutual positions (see Fig. 3). The diffraction studies of Birringer and Gleiter [2] and Zhu et al. [92] may serve as an experimental verification of some disorder of the interfacial component in nanomaterials fabricated by compaction.

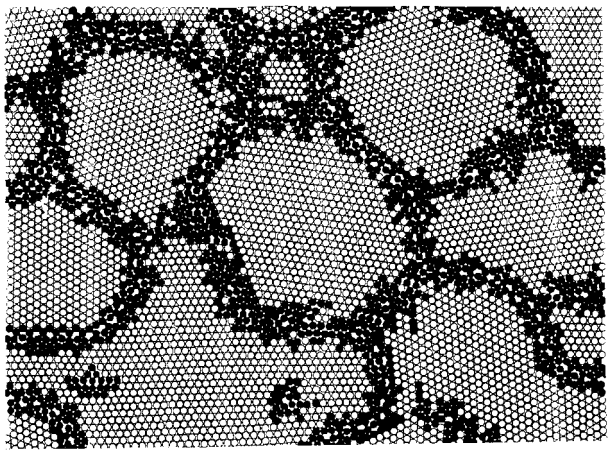

Figure 3. Two-dimensional model of the atomic structure of a nanocrystalline material calculated via the Morse potential: ○ are the crystallite atoms, • are the atoms of the interfaces shifted with respect to the sites of an ideal crystal lattice by more than 10 percent; chemically all the atoms are identical [86].

At the same time, recent studies [93–97] have revealed that the structure of the grain boundaries in nanomaterials is close to that in ordinary polycrystals and that the degree of order in the mutual position of atoms in grain boundaries is much higher than was assumed previously. The application of high-resolution electron microscopy [98] has shown that in nanomaterials, just as in ordinary polycrystals, the atoms in the interfaces are influenced only by two neighboring crystallites. Pores were discovered only at triple junctions rather than along the entire length of the grain boundaries; the number density of atoms in intercrystallite boundaries proved to be the same as in the crystallites.

The authors of [88, 89, 93, 94] were the first to report on the high degree of order in the position of atoms in the grain boundaries in samples of nanocrystalline compacted palladium nc-Pd. To analyze the experimental data on x-ray diffraction and x-ray absorption spectroscopy (extended x-ray absorption fine structure, or EXAFS) of nanocrystalline materials, Löffler et al. [95, 96] used the following distribution function for the atomic density:

$$\rho(r) = x_l \rho_l(r) + (1 - x_l)\langle\rho\rangle_{\mathrm{gb}}\,, \tag{2}$$

where r is the interatomic distance, x_l is the fraction of atoms occupying the sites of the crystal lattice, $\rho_l(r)$ is the distribution function for the atomic density in a nanocrystal in which the atoms belonging to the outer layers of a crystallite are at the lattice sites, and $\langle\rho\rangle_{\mathrm{gb}}$ is the atomic density of a grain boundary in which all the atoms occupy random positions not corresponding to the sites of the crystal lattice. The value of x_l can be found if we know the experimental distribution function for the atomic density, $\rho(r)$. To this end, using the function $\rho(r)$, we construct the dependence of the relative coordination number Z_i/Z_i^{ideal} (Z_i is the experimentally determined number of atoms on the ith coordination shell, and Z_i^{ideal} is the coordination number of the ith coordination shell of an ideal crystal) on the interatomic distance r. The limit value Z_i/Z_i^{ideal} at $r = 0$ corresponds to x_l, the fraction of atoms occupying the sites of the crystal lattice.

Figure 4 depicts the distribution function for the atomic density in a sample of nanocrystalline compacted palladium (nc-Pd) aged at room temperature for four months. Löffler et al. [95] employed experimental data on x-ray diffraction to calculate the distribution function $\rho(r)$. Their analysis, which used the function $\rho(r)$, shows that both in nc-Pd samples aged at room temperature for several months and in the samples additionally annealed at 973 K after aging, the ratio Z_i/Z_i^{ideal} at $r = 0$, i.e., the value of x_l, is equal (within errors) to unity (Figs 5a and 5b). In the nc-Pd sample studied no later than ten days after compaction, 8 to 14% of the atoms are not at the lattice sites (Fig. 5c) and the degree of short-range order in their mutual positions is extremely low. These results show that immediately after the sample is compacted, the grain boundaries in nc-Pd are in a nonequilibrium state with low short-range order; this state is unstable even at room temperature, and over 120–150 days becomes an ordered

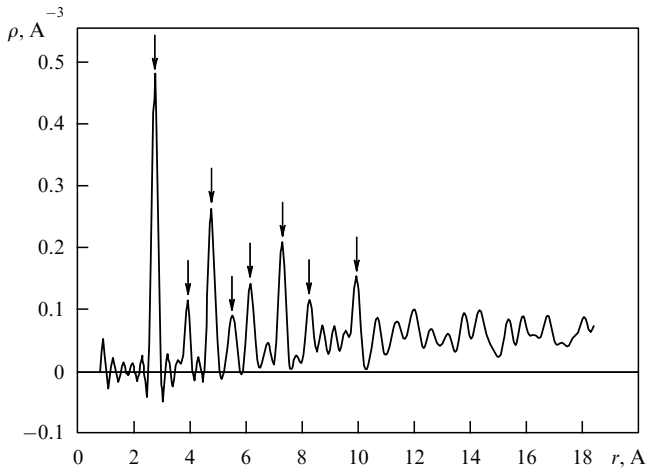

Figure 4. Atomic density distribution function for an aged nanocrystalline compacted palladium sample (nc-Pd) (the arrows indicate peaks corresponding to the first eight coordination shells) [95].

state; simultaneously the crystallite size increases from 12 to 25–80 nm (Fig. 6). The results reported in [95–97] indicate that the coordination number of the atoms belonging to grain boundaries in aged nc-Pd is close to that in ordinary coarse-grained polycrystalline palladium.

The study of vacuum-produced nanocrystalline compacted iron nc-Fe with an average crystallite size of 10 nm [99] revealed that $95 \pm 5\%$ of all the atoms are at the sites of the bcc lattice. In an earlier work, Zhu et al. [92] did not discover a perceptible short-range order in the positions of atoms in the grain boundaries of nc-Fe. Schlorke et al. [99] demonstrated that the unusual results of Zhu et al. [92] were due to the oxidation of the crystallite surface: in nc-Fe samples produced in an insufficiently high vacuum with residual oxygen, only $72 \pm 5\%$ of the atoms occupy the sites of the iron bcc lattice; the majority of the remaining atoms belong to the amorphous oxide phase, and only a small amount (5%) of iron atoms do not occupy the sites of the iron lattice.

Studies of short-range order in nanocrystalline compacted cobalt nc-Co [100] with an average crystallite size of 7 nm have shown that the samples contained a disordered amorphous phase ($\sim 70\%$) and an ordered crystalline phase ($\sim 30\%$). Babanov et al. [100] noted that the disordered phase occupying the grain boundaries had no specific features of a disordered gaslike phase. The relative content of the disordered phase in nc-Co is apparently strongly overestimated, since the nc-Co samples proved to be partially oxidized (the researchers report this fact themselves); besides, in processing experimental data, neither lattice defects nor free volumes were taken into account.

In reality, the interfaces of compacted nanocrystalline materials can carry three types of defects [5]: isolated vacancies; vacancy clusters or nanopores, which are formed in triple junctions of crystallites; and large pores in place of absent crystallites (Fig. 7). These defects are structural elements of the grain boundaries with reduced density.

Overlooking the presence of free volumes leads to large errors in determining the volume fraction of the interfacial component in nanocrystalline materials. For instance, studies of nc-Pd by small-angle neutron scattering [101] and the subsequent processing of the experimental data without allowing for porosity led to an erroneous conclusion that the volume fractions of crystallites and grain boundaries in nc-Pd

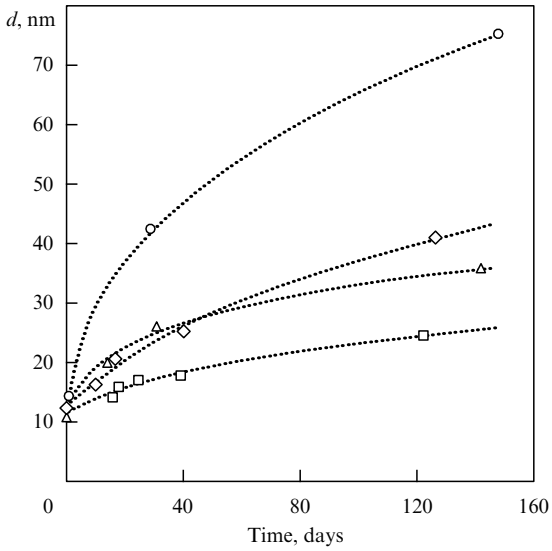

Figure 6. Changes in grain size in nc-Pd as a result of aging at room temperature [96].

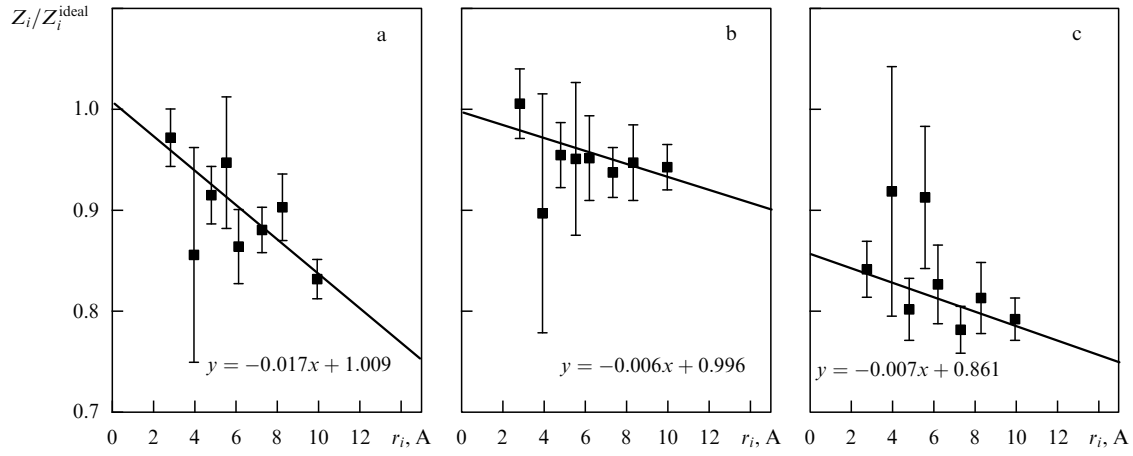

Figure 5. Dependence of the relative coordination number in nc-Pd samples on the interatomic distance r_i [95]: a, the nc-Pd sample after aging at room temperature for four months; b, the same aged sample after additional annealing at 973 K; and c, a freshly prepared sample of nc-Pd.

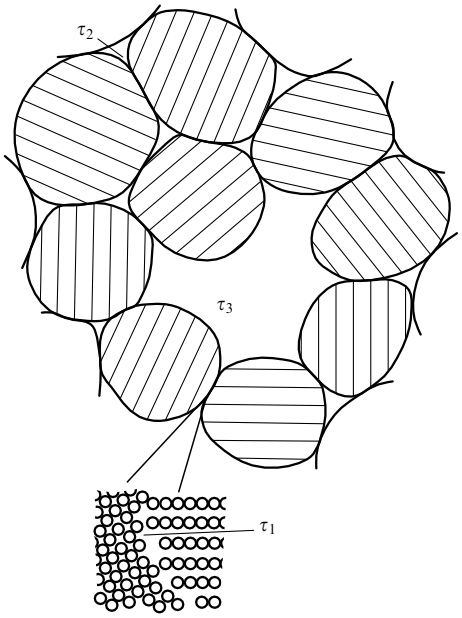

Figure 7. Two-dimensional model of a nanocrystalline material with microscopic free volumes, which can be detected by the positron annihilation method: a vacancy at a grain boundary (positron lifetime τ_1); a vacancy agglomerate (a nanopore) in a triple junction of crystallites (lifetime τ_2); and a large pore (lifetime τ_3) in place of an absent crystallite [5].

are 0.3 and 0.7, respectively; according to the estimate of Jorra et al. [101], the relative density of intercrystallite matter is only 50%. In a later study, Sanders et al. [102] investigated the properties of nc-Pd with a high degree of compaction and found that the density of the second phase reduces to zero. This means that the scattering objects are pores rather than grain boundaries with reduced density. Comparing the data of [101] and [102] with their own results, Weissmüller et al. [96] concluded that small-angle scattering can provide information about the grain boundaries with the exception of free volumes.

The most reliable method of studying free volumes in nanocrystalline compacted materials is positron annihilation spectroscopy [5, 103]. Lapovok et al. [104] were the first to use this method to study vacancies in nickel nanoparticles ($d \approx 15$ nm) by measuring the positron lifetime. In defect-free metals, positrons annihilate from a free state with a characteristic lifetime $\tau_f \sim 100$ ps. Positron capture by defects such as vacancies, vacancy clusters (nanopores), and pores leads to an increase in positron lifetime; the lifetime can be used to determine the type of defect (see Fig. 7). The larger the defect, the longer the positron lifetime. The existence of vacancies and nanopores was discovered by the positron annihilation method in nanocrystalline such metals as Al, Cu, Pd, Fe, and Ni, in nanocrystalline silicon, and in zirconium oxide ZrO_2 [5, 103, 105–109].

The results of these investigations imply that three components can be distinguished in the positron lifetime spectra: two strong and one weak, with intensities I_1, I_2, and $I_3 = 1 - I_1 - I_2$, respectively, and with corresponding lifetimes τ_1, τ_2, and τ_3 (Table 1). In nanocrystalline metals, the value of the lifetime τ_1 is close to that of the lifetime τ_{1V} of positrons in lattice monovacancies of coarse-grained metals,

Table 1. Positron lifetimes τ_1, τ_2, and τ_3 in nanocrystalline materials produced by evaporation and compaction (1), sputtering and compaction (2), and intense plastic deformation (3) and the average positron lifetime in nanocrystalline alloys produced by crystallization of amorphous alloys (4) [5, 103, 109–111]. For comparison we give the free-state positron lifetime τ_f of a defect-free crystal and the lifetime of positrons in lattice monovacancies, τ_{1V}, and in complexes consisting of i vacancies, τ_{iV}; d is the crystallite size.

Material	Production mode	d, nm	τ_1, ps	τ_2, ps	τ_3, ps	I_1	I_2	τ_f, ps	τ_{1V}, ps	τ_{iV}, ps [112]
Al	1	40	253 ± 4	412 ± 7	1970 ± 160	0.58	0.41	163 [108]	251 [108]	422 ($i = 13$)
Fe	1	10	161 ± 8	337 ± 6	900 ± 40	0.20	0.75	106 [108]	175 [108]	334 ($i = 10$)
Ni	1, 2	12	174 ± 1	363 ± 2	530 ± 70	0.28	0.72	94 [108]	180 [113]	376($i = 13$)
Cu	1	20	175 ± 10	299 ± 40	470 ± 50	0.43	0.44	112 [108]	179 [108]	
Cu	2	14	182 ± 8	311 ± 13	600 ± 200	0.40	0.59			
Pd	1	12	182 ± 5	347 ± 5	1080 ± 170	0.33	0.66	108 [114]	115 [109]	
Pd (measured in vacuum)	1	20	211	465		0.59	0.41	108 [114]		
Pd (measured after exposure to air)	1	20	186	365		0.47	0.53	108 [114]		
Pd (compaction under a pressure of 2 GPa at 373 K)	1	29	161	316		0.40	0.60	108 [114]		
Pd (pulverization in a ball mill)	1	86	202	359		0.90	0.10	108 [114]		
Pd										
Mo	3	76	172	398		0.96	0.04	108 [114]		
Cu	2	10	204 ± 9	345 ± 2		0.16	0.84	103 [108]	180 [108]	321($i = 9$)
Ni	3	$\geqslant 100$	171 ± 2	297 ± 9		0.83	0.17			
Si	3	200	161 ± 1	330 ± 9		0.88	0.12			
Pd_3Fe	1	10	314 ± 35	422 ± 11	3300 ± 300	0.20	0.79	219 [115]	272 [115]	272($i = 8$) [116]
NiZr	2	9	170 ± 8	351 ± 3		0.16	0.84	108(Pd) [114]		
ZrO_2	2	20	189 ± 2	415 ± 6		0.79	0.21	142 [108]		
	2	10	199 ± 2	378 ± 1	14500 ± 600	0.31		175 [117]		

Alloys	Production mode	$\bar{\tau}$, ps (nanocrystalline)	$\bar{\tau}$, ps (amorphous)	$\bar{\tau}$, ps (coarse-grained)
$Co_{33}Zr_{67}$	4	191 ± 1	187 ± 1	148 ± 1
$Fe_{90}Zr_{10}$	4	158 ± 1	158 ± 1	145 ± 1
$Fe_{73.5}Cu_1Nb_3Si_{13.5}B_9$	4	145 ± 1	151 ± 1	114 (Fe_3Si)

so that τ_1 is considered to be the lifetime of positrons in vacancies at grain boundaries; the size of these vacancies corresponds one or two removed atoms. That these free volumes belong to grain boundaries rather than to crystallites follows from the fact that the lifetime τ_1 is observed in nanocrystalline metals even after they have been annealed at a temperature higher than the annealing temperature of lattice monovacancies. The positron lifetime τ_2 characterizes positron annihilation in three-dimensional vacancy clusters (nanopores), whose size is approximately equal to the volume of ten absent atoms.

The lifetimes τ_1 and τ_2 of positrons in the SMC metals Cu, Pd, and Ni (Table 1) are close to the values τ_1 and τ_2 for the corresponding nanocrystalline metals. However, for the SMC metals the contribution of the second component, I_2, to the positron lifetime spectrum is much smaller, since the crystallites in SMC metals are larger than in nanocrystalline metals.

The extremely long positron lifetime τ_3 corresponds to positron annihilation in pores — large free volumes of a size close to that of a crystallite.

The annealing of n-Pd at $700 > T > 400$ K leads to an increase in the average positron lifetime because separate free volumes combine and there size increases; such structural relaxation of interfaces is accompanied by an increase in the density of these regions. At higher annealing temperatures the crystallites grow, and at $T > 1200$ K the average crystallite size already exceeds the positron's mean free path, so that the contribution of the free volumes, existing at interfaces, to positron annihilation decreases, and the lifetime drops to a value corresponding to the lifetime $\bar{\tau}$ of free positrons in coarse-grained metals. On the whole, the study of positron annihilation [5, 103, 105 – 109] in compacted nanocrystalline metals and alloys revealed the following:

(1) the lifetime of positrons in nanocrystalline metals is longer than the lifetime τ_f of free delocalized positrons;

(2) the fraction of positrons captured by vacancies increases with the pressure used in the compaction process, which means that by increasing the compaction pressure we increase the area of the interfacial component;

(3) positrons are captured by monovacancies, vacancy complexes, and pores whose size is close to that of crystallites;

(4) free (vacant) volumes that capture positrons belong to grain boundaries rather than to crystallites; and

(5) the capture of positrons by dislocations present in crystallites is unlikely, since plastic deformation of metals leads to a smaller change in the positron lifetime than does the production of metals in the nanocrystalline state by compaction.

3.2 Structure of submicrocrystalline metals

At present it is clear that the model of a gaslike structure does not reflect the real structure of grain boundaries in nanocrystalline materials. An alternative is the idea that the grain boundaries are in a nonequilibrium state and have an elevated energy due to the presence of dislocations directly in the grain boundaries and of uncompensated disclinations at triple grain junctions. The long-range stress field of the nonequilibrium grain boundaries is given by a strain tensor whose components inside a grain are proportional to $r^{-1/2}$, where r is the distance to the grain boundary. Hence, the stress field results in elastic distortions of the crystal lattice, whose magnitude is at its maximum near the grain boundary. This model was first proposed by a large group of researchers [65, 66, 118 – 121], who used it in their studies of SMC materials produced by different variants of the method of intense plastic deformation.

Electron-microscopic studies show that the main feature of the structure of SMC materials is the presence of randomly misoriented nonequilibrium grain boundaries. A characteristic feature of unannealed SMC metals and alloys is the presence of extinction contours in the grains (along their boundaries), which suggests the presence of high elastic stresses [64 – 67, 70 – 72]. Since the dislocation density inside grains is much lower than in the interfacial regions, we can conclude that it is the nonequilibrium grain boundaries that are the main source of elastic stresses. After annealing, many grains become free of dislocations, the extinction contours disappear, and a fringe contrast typical of an equilibrium state appears at the grain boundaries. This suggests that these boundaries have undergone relaxation. Another indication of the presence of elastic stresses in the grain boundaries are the experimentally observed local distortions of the crystallite lattice near the crystallite boundaries [88]. As a result of their Mössbauer spectroscopy studies of SMC iron, Valiev et al. [74] found that the experimental spectrum is a superposition of two spectra corresponding to two different states of iron atoms. One of these (the state of iron atoms in crystallites) coincided with that of iron atoms in ordinary coarse-grained α-Fe. The second component of the experimental spectrum reflects the special state of the iron atoms in the grain boundaries, although the crystal structure of the grains and their boundaries is the same. According to Valiev et al. [65, 66], the difference in the parameters of the hyperfine structure of the Mössbauer spectra of SMC iron is due to the higher dynamic mobility of the atoms belonging to grain boundaries.

The results obtained by the positron annihilation method [111] (see Table 1) indicate a certain similarity between the microstructure of nanocrystalline and SMC materials; in particular, both contain free volumes of the same type.

The grain boundary model discussed in [118 – 124], which takes into account both dislocations and disclinations, makes possible a quantitative estimate of the generated stresses, the excess energy of grain boundaries, and the change in the crystallite volume caused by the excess elastic energy. According to Nazarov et al. [119], the mean-square stress $\varepsilon_{\rm disl}$ generated in a grain boundary (which is a disordered dislocation network) per unit grain boundary area is

$$\varepsilon_{\rm disl} \approx 0.23b\left(\frac{\rho}{d}\log\frac{R}{2b}\right)^{1/2} \approx 0.13b\left(\rho_V \log\frac{R}{2b}\right)^{1/2}. \quad (3)$$

The excess energy (per unit grain boundary area) caused by external dislocations $\gamma_{\rm ex,\,disl}$ is

$$\gamma_{\rm ex,\,disl} = Gb^2\rho\frac{\log(R/2b)}{4\pi(1-\nu)}. \quad (4)$$

In Eqs (3) and (4), b is the Burgers vector, d is the grain size in the nanocrystal, ρ and $\rho_V \approx 3\rho/d$ are the linear and volume dislocation densities, R is grain size in an ordinary polycrystal, G is the shear modulus, and ν is the Poisson ratio. High internal stresses lead to a change in the volume of the SMC material:

$$\frac{\Delta V}{V} \approx 0.13b^2\rho_V \log\frac{R}{2b}. \quad (5)$$

Similar equations for a system of disclinations formed at the junction of several grains have been derived in the two-

dimensional model of a polycrystal with square grains [122]:

$$\varepsilon_{\text{discl}} \approx 0.1\langle\Omega^2\rangle^{1/2}, \tag{6}$$

$$\gamma_{\text{ex, discl}} = G\langle\Omega^2\rangle \frac{d \log 2}{16\pi(1-\nu)}, \tag{7}$$

where $\langle\Omega^2\rangle$ is the mean-square disclination strength.

According to Rybin et al. [125], the disclination strength is $1-2^\circ$, so that $\langle\Omega^2\rangle^{1/2} \approx 0.03$. The bulk dislocation density ρ_V in SMC materials amounts to 3×10^{15} m^{-2} [119]. Bearing all this in mind, we can arrive at the following numerical estimates: for SMC aluminum with 100-nm grains, $\gamma_{\text{ex, disl}} \approx 0.3$ J m^{-2} and $\gamma_{\text{ex, discl}} \approx 0.06$ J m^{-2}. The increase in the volume due to the presence of dislocations amounts to $\Delta V/V \approx 4 \times 10^{-4}$. Since the change in volume is proportional to the elastic energy and $\gamma_{\text{ex, discl}}$ is five times smaller than $\gamma_{\text{ex, disl}}$, the increase in the volume due to the presence of disclinations is $\sim 0.8 \times 10^{-4}$. The total increase in the volume of SMC aluminum amounts to $\Delta V/V \approx 4.8 \times 10^{-4}$, which is smaller than the experimental value $\Delta V/V \approx 9 \times 10^{-4}$ by a factor of two. Apparently, the additional increase in the volume is due to the formation of vacancies in the deformation process.

For SMC copper with a grain size $d = 200$ nm at $\rho_V \approx 3 \times 10^{15}$ m^{-2} and $\langle\Omega^2\rangle^{1/2} \approx 0.03$, an estimate via Eqns (3)–(7) yields $\varepsilon_{\text{disl}} \approx 7.5 \times 10^{-3}$, $\varepsilon_{\text{discl}} \approx 3 \times 10^{-3}$, a total internal elastic stress $\varepsilon = (\varepsilon_{\text{disl}}^2 + \varepsilon_{\text{discl}}^2)^{1/2} \approx 8 \times 10^{-3}$, $\gamma_{\text{ex, disl}} \approx 0.41$ J m^{-2}, $\gamma_{\text{ex, discl}} \approx 0.09$ J m^{-2}, and $\gamma_{\text{ex}} = \gamma_{\text{ex, disl}} + \gamma_{\text{ex, discl}} \approx 0.5$ J m^{-2}. The value of ε found agrees fairly well with the results of the investigation of internal stresses in SMC copper by the x-ray diffraction method [120].

The model developed in [121–123] takes into account the important role of disclinations forming at triple grain junctions. Here the splitting of disclinations, studied by Gutkin et al. [123, 124], is important. The splitting of disclinations at triple junctions lowers the system's elastic energy. Such splitting into weaker disclinations may be of a volume nature (Fig. 8b); in this case the triple junction region becomes locally amorphous. Another variant is the splitting of a disclination into three series of weaker disclinations along the boundaries of neighboring grains (Fig. 8c). Also, linear splitting of a disclination into a series of weaker disclinations along the grain boundary is possible (Fig. 8e).

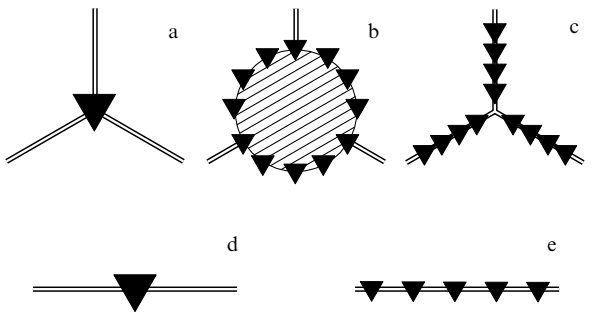

Figure 8. Splitting of disclinations at (a) a triple junction and (d) an intercrystallite boundary; (b) depicts the splitting of the initial disclination into an ensemble of weaker disclinations, with a region of local amorphization being formed at the triple junction; (c) depicts the splitting of an initial disclination into three series of weaker disclinations positioned along the intercrystallite boundaries; and (e) depicts linear splitting of a disclination in a grain boundary [123].

According to Gutkin et al. [123, 124], the greater the number of new disclinations, the lower the elastic energy of the initial grain boundary disclination. In the case of linear splitting, the largest decrease in the elastic energy is achieved when the two new disclinations that are formed are separated by the maximum possible distance, i.e., the grain-boundary length between nearest functions. The splitting of disclinations in grain boundaries of nanocrystalline materials is an efficient relaxation channel for the elastic energy, is accompanied by changes in the structure of the grain boundaries (the emergence of stacking faults), lowers the probability of nucleation of microcracks near a grain boundary, and stimulates grain-boundary diffusion.

On the whole, the results of experimental and theoretical studies of grain boundaries suggest that the presence of a long-range field of elastic stresses constitutes (in addition to the small grain size and large extension of grain boundaries) the main feature of nanocrystalline materials.

The ideas concerning the microstructure of nanocrystalline materials are mainly based on the results of x-ray diffraction studies of lattice parameters, internal stresses, and atomic displacements. In comparison with coarse-grained materials, x-ray diffraction patterns of nanocrystalline materials depict a larger width of reflections, a change in their shape, and a displacement of their position. Broadening of the diffraction maxima is due to the small grain size and microdeformations (stacking faults) of the crystal lattice; the shape and intensity of the reflections depend on the magnitude of atomic displacements; and the shift of reflections indicates a change in the lattice parameters. Important data on the structure can be extracted by analyzing the background, which originates from thermal diffuse scattering, the absence of order in the positions of atoms in the amorphized matter, and diffuse scattering by the solid solution. Thermal diffuse scattering causes the background intensity to increase monotonically with the reflection angle θ, while the absence of atomic order leads to a monotonic decrease in the background intensity. The presence of short-range order due to the beginning ordering or, on the contrary, a segregation leads to periodic variations in the background intensity [127].

According to experimental data, a decrease in grain size in nanocrystalline materials can lead both to a decrease [128–131] and an increase [131–133] in the values of the lattice parameters. A decrease is more probable, and this feature can be observed when crystallites are smaller than 10 nm. The increase of the lattice parameter noted by some researchers is most probably due to adsorption and dissolution of impurities by the crystallite surface, as is the case for isolated nanoparticles; e.g., for small MgO particles with a clean surface, the lattice parameter becomes smaller, whereas adsorption of water results in an increase in the lattice parameter [21, 134].

A broadening of diffraction lines is observed in all nanocrystalline materials. The broadening β_s associated with the small size d of the crystallites is described by the following formula:

$$\beta_s(2\theta) = \frac{k\lambda}{d\cos\theta}, \tag{8}$$

where $k \approx 1$ is the crystallite's shape factor. The deformation broadening β_d associated with stacking faults can be

calculated by the formula

$$\beta_{\rm d}(2\theta) = 2A\langle\varepsilon^2\rangle^{1/2}\tan\theta\,, \tag{9}$$

where A is a parameter approximately equal to unity when the distribution of dislocations in the crystallite is uniform; in (8) and (9) the broadening β is expressed in radians.

Due to the different dependence of the size and deformation broadenings on the order of reflection, we can separate these contributions by using pairs of diffraction reflections (hkl) differing only in reflection order and the formula

$$\beta \approx 0.5\left[\beta_{\rm s} + (\beta_{\rm s}^2 + \beta_{\rm d}^2)^{1/2}\right], \tag{10}$$

where β is the total broadening of the diffraction reflection; we assume, when performing separation, that $\beta_{\rm s}$ is independent of l. The separation of the size and deformation broadenings shows that the mean-square deformation in nanocrystalline Al, Ru, Pd, Cu, and AlRu [93, 129, 135, 136] amounts to 1 – 3% and is much larger than for coarse-grained metals.

A detailed analysis of the results of x-ray diffraction studies of nanocrystalline materials can be found in Aleksandrov and Valiev's paper [137].

The problem of computer simulation of the x-ray diffraction pattern of nanocrystalline materials [138 – 141] allowing for the grain size, the distortions of the crystal lattice, and the thickness and structure of the grain boundaries is of interest. The problem can be solved by using the kinematic scattering theory in connection with x-ray scattering. A polycrystal is taken that contains 361 cubic crystallites; the length of the crystallite edge is Na, with a the parameter of the unit cell. The crystallite size was varied by changing the number of particles, N. In calculations of atomic displacements it was assumed that all atoms of the outer layers of the crystallites are shifted at random from their positions in an ideal lattice and that the magnitude of the displacements varies from 0 to $0.5b$, with $b = a/\sqrt{2}$ being the Burgers vector.

Alexandrov and Valiev's calculations [138, 139] show that the atomic displacements at the crystallite surface only reduce the intensity of diffraction lines, i.e., have no effect on the shape, width, and position of the reflections. A decrease in crystallite size appreciably broadens the diffraction reflections. The effect of the long-range field of elastic stresses on the reflection parameters was modeled by changing the linear dislocation density ρ in grain boundaries. With increasing dislocation density from 0 to 0.1 and 1.0 nm^{-1}, reflections become broader and shift to the range of larger angles θ. At $\rho = 0.1$ nm^{-1}, the size effect of broadening is predominant when crystallites are smaller than 30 lattice parameters ($d < 30a$). For larger crystallites the main contribution to the broadening of reflections is provided by elastic distortions of the crystallite lattice caused by dislocations in grain boundaries. This implies that the effect of elastic stresses in grain boundaries on the microstructure of nanomaterials weakens as the crystallites become smaller.

4. Effect of grain size and interfaces on the properties of compact nanomaterials

In order to theoretically interpret the experimental data obtained in studies of compact nanocrystalline materials it is important that surface effects (i.e., effects related to grain boundaries) are separated from volume effects (i.e., effects related to the particle size). There is still a long way to go before this problem is solved, since at the present time the study of compact nanomaterials (which began a decade ago) is still in the stage of intensive experimental data gathering. For this reason the level of theoretical explanation of the structure and properties of compact nanocrystalline materials is much lower than for isolated nanoparticles.

4.1 Anomalies of mechanical behavior

An outstanding property of nanocrystalline materials is that they are extremely hard. Hardness is the resistance of a material to elastic and plastic deformation on indentation and is determined to a great extent by the material's yield strength. The grain size strongly affects the yield strength $\sigma_{\rm y}$; this effect has been thoroughly studied in metals, alloys, and ceramic materials with grains greater than $d = 1$ μm. According to the Hall – Petch law [142, 143],

$$\sigma_{\rm y} = \sigma_0 + k_{\rm y} d^{-1/2}\,, \tag{11}$$

where σ_0 is the internal stress impeding dislocation motion, and $k_{\rm y}$ is a constant. At temperatures $T/T_{\rm m} < 0.4 - 0.5$, where $T_{\rm m}$ is the melting point, the hardness $H_{\rm V}$ (Vickers microhardness) is related to the yield stress $\sigma_{\rm y}$ through the empirical relationship $H_{\rm V}/\sigma_{\rm y} \approx 3$ [144]. This leads to the following size dependence of hardness:

$$H_{\rm V} \approx H_0 + k d^{-1/2}\,, \tag{12}$$

where H_0 and k are constants.

If deformation is effected by diffusion-controlled creep, then, according to Coble [145], at moderate temperatures $T/T_{\rm m}$ the deformation rate is

$$\dot{\varepsilon} = \frac{B\sigma\Omega\delta D}{k_{\rm B} T d^3}\,, \tag{13}$$

where B is a proportionality factor, σ is the applied stress, Ω is the atomic volume, δ is the thickness of the grain boundary, and D is the grain-boundary diffusion coefficient.

Equations (11) – (13) imply that a decrease in grain size leads to an appreciable change in mechanical properties. In particular, Eqns (11) and (12) predict that the material's strength grows as d decreases. At the same time, Eqn (13) suggests that, for nanometer grains, diffusion-controlled creep is important even at room temperatures, and increases the deformation rate considerably. Thus, the effect of grain size on the strength of a nanocrystalline material is ambiguous and depends on the relationship between the yield strength and the deformation rate. Moreover, one must take into account the possible increase in the grain-boundary diffusion coefficient D as the grains get smaller.

At 300 K the microhardness of nanocrystalline materials is two to seven times greater than the $H_{\rm V}$ of coarse-grained materials.

The data from the literature on the grain-size dependence of the microhardness of nanocrystalline materials are contradictory. Chokshi et al. [146] were the first to study the effect of grain size on the microhardness of nanocrystalline materials (copper and palladium). They found that a decrease in grain size for coarse-grained copper from 25×10^3 to 5×10^3 nm is accompanied by an increase in microhardness. The microhardness of nanocrystalline copper nc-Cu ($d \approx 16$ nm) was found to be approximately 2.5 times larger than that of

copper with a grain size of 5×10^3 nm, but as the grain size of nc-Cu dropped from 16 to 8 nm, H_V decreased by roughly 25%. A decrease in H_V was also observed as the grain size of nc-Pd dropped from 13 to 7 nm. Chokshi et al. [146] explained the decrease in the microhardness of nc-Cu and nc-Pd by the much higher (in comparison to coarse-grained metals) deformation rate $\dot{\varepsilon}$.

A decrease in H_V of the nanocrystalline alloys Ni–P, TiAlNb, and $NbAl_3$ caused by a drop in grain size from 60–100 to 6–10 nm was discovered by the authors of [147–150]. They believe that the effect is caused by the increase in the contribution of diffusion mobility to the deformation process as d gets smaller. An increase in H_V caused by a drop of grain size of nc-Cu, nc-Fe, and nc-Ni was observed by a number of researchers [146, 151–153].

An interesting fact was reported by Fougere et al. [154]. They found that H_V increases or decreases depending on which method is used to measure the grain size. The hardness increases as H_V drops when measurements are made using different samples with different grain sizes. On the other hand, H_V increases with d to a certain value, and then a decrease in H_V is usually observed, when the measurements involve the same sample, in which the grain size grows under annealing. For instance, initial annealing at 569 K of compacted nc-Pd for 60–90 min leads to grain growth and an increase in hardness by 7–11%; longer annealing, which leads to further grain growth, is accompanied by a decrease in hardness. The microhardness of compacted nc-Cu was found to grow by 4–5% in the course of the first 20–30 min of annealing at 423 K and then decreased (Fig. 9) [154].

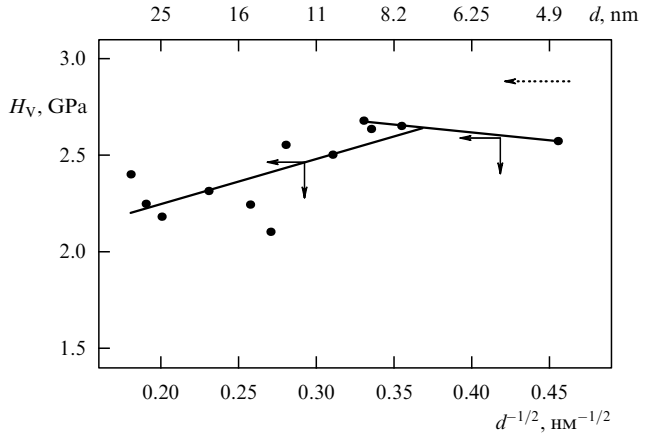

Figure 9. Dependence of the microhardness H_V of compact nanocrystalline copper nc-Cu on $d^{-1/2}$, where d is the grain size [154]: the growth of nc-Cu grains was achieved by increasing the time of annealing at 423 K (the dashed arrow points in the direction of an increasing annealing time).

The results of hardness measurements of the nanocrystalline metals Ag, Cu, Pd, Se, Fe, and Ni in samples with different grain sizes were generalized by Siegel and Fougere [155]: a decrease in d to 4–6 nm is accompanied by a growth in hardness. The hardness of intermetallic compounds and alloys in which the grain size was varied by annealing depends on d in a more complicated manner: first an increase in d leads to an increase in H_V followed by a decrease [155].

According to Siegel and Fougere [155] and Hahn and Padmanabhan [156], the fact that the experimental data on the size dependence of the hardness of nanomaterials are discrepant may follow from the different structure of grain boundaries. In view of this, the results of studies [66, 157] of the microhardness of the SMC alloys $Al_{98.5}Mg_{1.5}$ are of interest. They indicate that even when the grain size remains unchanged ($d \approx 150$) nm, a decrease in the extent to which the grain boundaries are nonequilibrium, achieved by annealing, has a strong effect on the microhardness. According to electron-microscopic data, annealing of the SMC alloy $Al_{98.5}Mg_{1.5}$ ($d \approx 150$ nm) at 400 K results in a relaxation of grain boundaries and a gradual transition to an equilibrium state, although the grain size remains unchanged. The relaxation of grain boundaries was found to be accompanied by a drop in microhardness from 1.7 to 1.4 GPa.

To find the relaxation temperatures in nanomaterials, measurements of H_V at 300 K after annealing at a certain temperature are used. Akhmadeev et al. [67] and Rempel' et al. [68] studied the effect of the annealing temperature on H_V and the structure of SMC Cu with average grain sizes of 200–300 nm and 130–160 nm. The microhardness of the initial and SMC copper was 1.2 and 1.4 GPa, respectively. Annealing at $T < 400$ K was found to have no appreciable effect on the structure and microhardness. A sudden drop in the microhardness of SMC Cu by a factor of two to three occurred after annealing at 425 – 450 K and was related to grain growth, the relaxation of internal stresses, and the lowering of the dislocation density, i.e., to an irreversible transition from the submicrocrystalline state to a coarse-grained state.

Rempel' et al. [70 – 72] measured the microhardness of SMC Pd with an average grain size of 150 nm by the method of torsion under quasihydrostatic pressure and found it to be 2.1 GPa. Annealing resulted in a decrease in microhardness, with a sudden drop occurring after annealing at 475 K (Fig. 10). A sudden decrease in microhardness by a factor of almost three after annealing at 475 – 600 K is related, as shown by electron-microscopy, to grain growth and partial annealing of dislocations.

The annealing of nc-Ag samples ($d \approx 10$ nm) prepared by compaction of nanoclusters was accompanied by a gradual

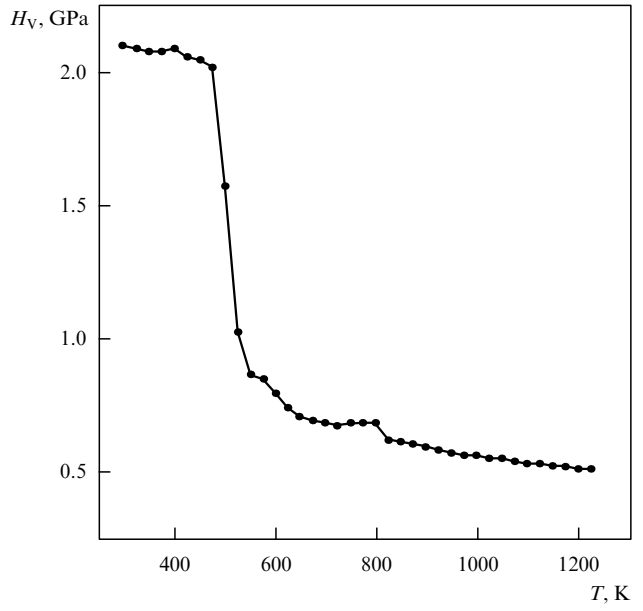

Figure 10. Variation of the microhardness of SMC Pd measured at 300 K as a function of the annealing temperature T [71].

reduction of microhardness from 1.5 to 0.3 – 0.5 GPa; no sudden drop in H_V was observed [98]. The decrease in H_V and grain growth started after annealing at 370 K. In contrast to nc-Ag, the annealing of samples of nanocrystalline magnesium oxide nc-MgO ($d \approx 10$ nm) up to 870 K is not accompanied by changes in microhardness, which amounts to 2.5 ± 0.2 GPa at 870 K [158]. The different behavior of the microhardness of a nanocrystalline metal (nc-Ag) and a nanocrystalline ceramic material (nc-MgO) upon annealing (Fig. 11) indicates the much higher structural stability of the nanocrystalline ceramic material and the conservation of grain size in such a material up to 800 – 900 K. Interestingly, the annealing of nc-MgO at $870 < T \leqslant 1070$ K resulted in a 30% increase in microhardness.

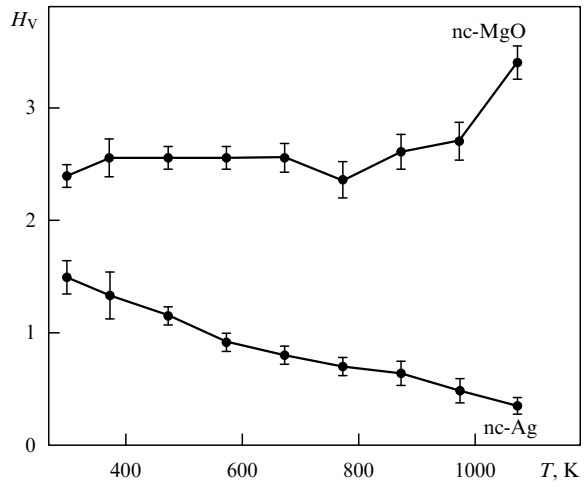

Figure 11. Variation of the microhardness H_V of compact nanocrystalline silver nc-Ag and magnesium oxide nc-MgO caused by annealing [98].

According to He and Ma [159], the microhardness of nc-Cu and nc-Fe produced by hot pressing of nanopowders at 723 – 773 K under a pressure of 0.64 GPa is four times greater than H_V for coarse-grained copper and iron. The microhardness of the nanocomposite material $Cu_{1-x}Fe_x$ ($d = 25$ – 45 nm) prepared by intense milling of copper and iron powders followed by hot pressing is 40 – 50% higher than the expected additive hardness H_V of the mechanical mixture. The same increase in H_V was observed in the nanocomposite materials Cu – W and Cu – Nb [160, 161]. According to He and Ma [159], the increase in the hardness H_V of the nanocomposite material Cu – Fe is due to the formation of grain boundaries with an elevated dislocation density, since copper and iron have different structures (fcc and bcc, respectively).

Measurements of the velocities of longitudinal and transverse ultrasonic waves in SMC Cu as a function of the annealing temperature made it possible to estimate the elasticity modulus E and the shear modulus G [162]. The size of SMC-Cu grains prior to annealing was 200 – 400 nm. Annealing was done in the 373 – 623 K range in steps of 25 – 50 K for one hour at each temperature. The values of E and G of the initial SMC Cu were 10 – 15% lower than those of coarse-grained copper. Earlier the reduced (by approximately 30%) values of the elastic moduli were obtained by Neiman et al. [136] and Korn et al. [163]. These researchers observed a sudden increase in E and G at annealing temperatures in the 423 – 456 K range (Fig. 12). Akhmadeev et al. [162] explained these variations in the elastic moduli by changes in the structure of grain boundaries: in SMC-Cu samples with grains of approximately 200 nm in diameter, the grain boundaries were in a nonequilibrium state and had excess energy. Annealing at $T \geqslant 423$ K was found to lead to relaxation of grain boundaries.

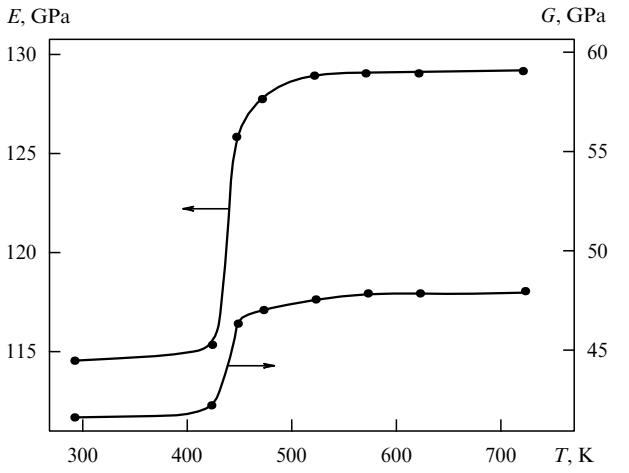

Figure 12. Effect of the annealing temperature T on the elastic modulus E and the shear modulus G of SMC copper measured at 300 K [162].

Lebedev et al. [164] studied the effect of temperature on the elasticity modulus E of SMC copper produced by compacting nanoparticles ($d \approx 80$ nm) and by the equichannel corner extrusion ($d \approx 200$ nm). Copper produced by compacting nanopowders under a pressure of 1 GPa had a porosity of roughly 11%. It was found that the elasticity modulus E of compacted copper increases after annealing at $T \leqslant 470 – 520$ K and drops sharply after being annealed at 670 K because of grain growth and a simultaneous increase in the porosity of the compacted copper. As the annealing temperature is raised, the elasticity modulus of plastically deformed copper rapidly increases in the 370 – 500 K and 720 – 870 K ranges. Lebedev et al. [164] explained the jump in E after annealing at 370 K by the pinning of grain-boundary dislocations by point defects and by the lowering of the dislocation mobility due to changes in the structure of grain boundaries, while the second jump was explained by the disappearance of the interfacial phase as a result of grain growth.

On the whole, the results of the authors of [162 – 164] suggest that the unusual elastic properties of SMC metals are due not only to the small size of grains but also to the state of grain boundaries.

Grain refinement is a common method of raising strength of materials. Neiman et al. [136] studied the stress – strain diagrams for compacted samples of nanocrystalline palladium ($d = 5 – 15$ nm) and nanocrystalline copper ($d = 25 –$ 50 nm) and found that the yield stress σ_y of nanocrystalline metals is two to three times greater than for coarse-grained metals. Valiev et al. [64] discovered a significant increase in σ_y of SMC magnesium alloys compared to the values for coarse-grained alloys. The tensile strength of nanocrystalline metals is 1.5 to 8 times higher than for coarse-grained metals [136, 155]. According to Neiman et al. [136], the main reasons for

the increase in the strength of nanocrystalline metals may be the difficulties (caused by the small grain size) in the formation and growth of dislocations or high residual stresses. The changes in the strength of materials caused by the transition to the nanocrystalline state require detailed study.

An important problem is the damping of vibrations of metallic materials. The improvement of damping properties reduces the harmful effect of cyclic loads, which are the cause of many accidents and breakdowns, lowers the noise caused by the vibrations of mechanisms, and raises the accuracy of measuring devices. Mulyukov et al. [165–169] studied the amplitude dependence of internal friction in SMC Cu and found that the smaller the crystallites and the greater the deviation of grain boundaries from the equilibrium state, the higher the background of internal friction and the better the damping properties of the material. For instance, in SMC Cu with an average grain size of roughly 200 nm that has been annealed at 423 K, the background level is three to five times higher than that in gray cast iron (the background level for gray cast iron is a nominal limit for heavy damping). The temperature at which internal friction begins its sharp rise in SMC Cu lowers by approximately 100 K in comparison to the value for coarse-grained copper. More than that, at 475 K a pronounced maximum appears in the internal friction. This raises the internal friction of SMC Cu approximately threefold in the temperature interval 240 to 475 K in comparison to coarse-grained samples.

All these features are related to the difference between the elasticity moduli of grains and of grain boundaries noted by Valiev et al. [65, 66]. The difference in the moduli makes it possible to think of SMC materials as being nonuniform for wave propagation. In view of this, there is considerable scattering of elastic vibrations in SMC materials and improvement of the damping properties. Note that nanocrystalline and SMC materials combine enhanced strength [64, 136, 155] and damping properties [65, 66, 165–169]; ordinary materials become weaker as the damping properties improve.

This effect of simultaneous improvement of damping and strength properties discovered in SMC Cu was corroborated by the studies of stainless steel made by Mulyukov et al. [170, 171]. They found that the formation of an SMC structure in steel increases the internal-friction background and the yield stress fourfold.

The superplasticity of ceramic nanomaterials must also be mentioned. For a long time superplasticity was only a dream of materials scientists studying the processes that take place during deformation and casting of ceramic materials. Superplasticity is characterized by an exceptionally large relative elongation of the material under tensile stresses. Pearson [172] was the first to discover this effect in an Sn–B alloy, which increased its length under tensile stress more than twenty-fold. This happened in 1934. The superplasticity of ceramic materials was first discovered in 1985 by Wakai et al. [173], who used polycrystalline tetragonal oxide ZrO_2 stabilized by yttrium oxide Y_2O_3. Later superplasticity was observed in the two-phase composite ceramic material Si_3N_4/SiC [174] and in other ceramic materials.

The superplasticity of ceramic materials is very important for producing articles by casting, solid-phase sintering, and hot compaction at relatively low temperatures. Because of superplasticity, it is easy to achieve a high accuracy in producing ceramic articles that are extremely complicated in shape, with inner cavities and surfaces of varying curvature.

According to Sherby and Ruano [175], the superplasticity of ceramic materials manifests itself most vividly when the grains are smaller than 1 μm, with the requirement that the grain size remains unchanged as long as possible with rising temperature. For instance, in nanocrystalline compacted magnesium oxide nc-MgO, the grain size remains almost the same when annealed up to 800–900 K [158]. In zirconium oxide, as the temperature is raised, grain growth is suppressed by adding small amounts of Y_2O_3. In two-phase ceramic materials based on silicon nitride and silicon carbide, the growth of grains of the matrix phase is suppressed due to precipitation of grains of the second phase. The factors that increase the plasticity of ceramic materials are also large-angle misorientations at grain boundaries and the presence of small amounts of an amorphous grain-boundary phase [176]. In the nanocrystalline state, some ceramic materials (e.g., TiO_2 [177]) are already plastically deformable at room temperatures.

4.2 Thermophysical and electrical properties

In contrast to nanoparticles, for which surface and size effects observed in the phonon spectrum and in the behavior of heat capacity have been thoroughly studied, similar studies for compact nanocrystalline materials are limited to a few papers.

The heat capacity C_p of samples of nc-Pd ($d = 6$ nm) and nc-Cu ($d = 8$ nm) produced by compacting nanoclusters was measured in the temperature range 150–300 K by Rupp and Birringer [178]. The relative density of the nc-Pd samples amounted to 80% and that of the nc-Cu samples, to 90% of the density of the respective nonporous polycrystalline metal. Measurements revealed that the C_p of the nc-Pd and nc-Cu samples are 53% and 9–11% higher than those of ordinary polycrystalline palladium and copper, respectively (Fig. 13). When nc-Pd was heated at $T = 350$ K, an exothermic effect was observed and the grain size remained unchanged or increased to 10 nm; the heat capacity of nc-Pd heated to 350 K was found to exceed the heat capacity of coarse-grained palladium by 5%. Rupp and Birringer [178] assumed that the observed elevated heat capacity can be explained by the more loose structure of grain boundaries. Such an explanation in not really plausible since it is common knowledge that the structure of the grain boundaries in compacted nanomaterials differs little from the crystallite structure. More likely, the excess heat capacity can be explained in the same way as in nanopowders, i.e., by the large area of the grain boundaries and the corresponding contribution to the heat capacity. This statement can be corroborated by measuring the heat capacities of a nanopowder and a sample produced by compacting the same powder; surely, with the grain size being the same, the heat capacity of the nanocrystalline powder and that of the compacted nanomaterial are close (to within experimental error). Moreover, impurity hydrogen may contribute to the excess heat capacity; this is especially true of palladium, which can absorb and dissolve hydrogen very easily.

Indeed, in their study of heat capacity of nc-Pd, Tschöpe and Birringer [179] established that at roughly 300 K the majority of the excess heat capacity of compacted nanomaterials is due to the excitation of impurity hydrogen atoms. Impurity hydrogen is often present in nanomaterials produced by condensing nanoclusters in an inert gas and subsequent compaction. For instance, an elevated solubility of hydrogen in grain boundaries in nc-Pd was reported by

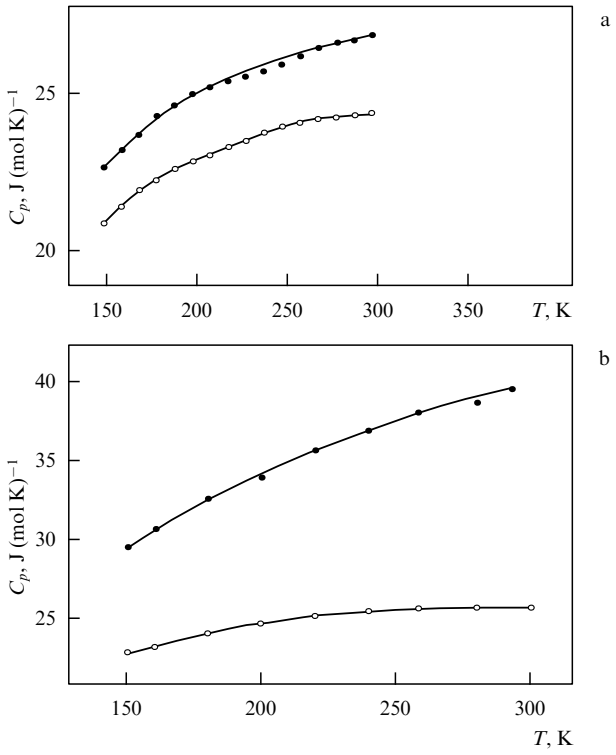

Figure 13. Effect of the nanocrystalline state on the temperature curves of the heat capacity $C_p(T)$ for copper and palladium: (•) heat capacity of nanocrystalline compacted copper nc-Cu and palladium nc-Pd; and (○) heat capacity of ordinary polycrystalline coarse-grained copper and palladium [178].

Mütschele and Kirchheim [90] and Stuhr et al. [180]. According to Eastmen et al. [181], the hydrogen is primarily dissolved in nc-Pd grains rather than in the grain boundaries.

Goll and Löhneyen [182] found that in the temperature range of 0.06 to 10.0 K the low-temperature heat capacity of samples of nanocrystalline compacted copper with grain sizes 6.0 and 8.5 nm is five to ten times larger than the heat capacity of coarse-grained copper. The greater increase in heat capacity was observed in the nc-Cu sample with the smaller grain size. The increase in the heat capacity of nc-Cu at $T > 1$ K may be explained by the fact that the loosely bound atoms at the grain surface behave like Einstein's linear oscillators and that surface vibrational modes appear in the phonon spectrum. According to Goll and Löhneyen's estimate [182], each 6th to 10th surface atom (depending on the particle size) is such an oscillator.

Trampenau et al. [183] used inelastic neutron scattering at 100 – 300 K to study the density of phonon states $g(\omega)$ in an n-Ni nanopowder, a nanocrystalline compacted nc-Ni sample with a relative density of 80%, and in coarse-grained nickel ($\omega = 2\pi\nu$ is the cyclic frequency). The grain size in both n-Ni and nc-Ni was about 10 nm. The most pronounced size effect was the increase in the phonon state density $g(\omega)$ of both n-Ni and nc-Ni samples in comparison to that of coarse-grained nickel in the energy range below 14 MeV (Fig. 14). According to Trampenau et al. [183], the change in the phonon spectrum of nc-Ni is due to the low density of matter at the grain boundaries, to which roughly 20% of the atoms belong. Calculations done on the basis of the data on the phonon state density revealed that the heat capacity of nc-Ni at $T \leqslant 22$ K is 1.5 to 2 times greater than the heat capacity of

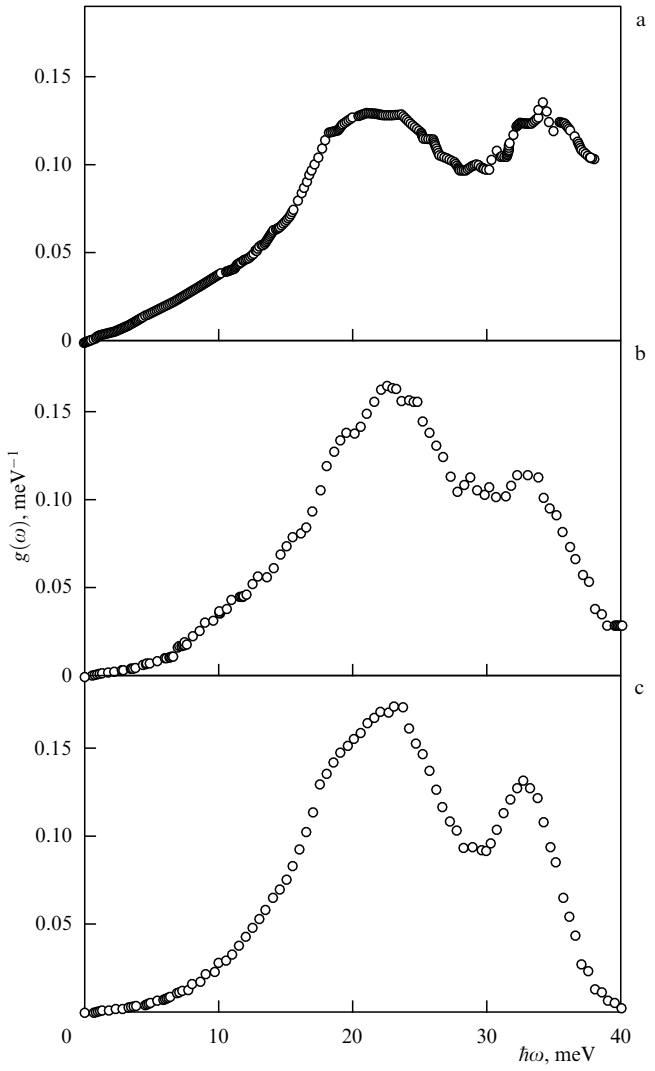

Figure 14. Phonon density of states of nanocrystalline nickel in compacted (a) and powder (b) states and of coarse-grained polycrystalline nickel (c) [183].

coarse-grained nickel. Trampenau et al. [183] also noticed that the excess heat capacity of compacted nanomaterials in the room-temperature range is most likely due to an admixture of hydrogen atoms, whose vibrations are excited at $T \geqslant 300$ K.

Measurements of the temperature dependence of the heat capacity of compacted samples of nanocrystalline nickel nc-Ni with an average grain size of roughly 70 nm [77] have shown that at $T \leqslant 600$ K nc-Ni has a much higher heat capacity than coarse-grained nickel. According to Valiev et al. [65, 77], the elevated heat capacity of nc-Ni is due to the contribution of the grain-boundary phase, which has a reduced Debye temperature and an elevated (by 10 – 25%) heat capacity compared to the values for the coarse-grained material.

To explain the anomaly of the low-temperature heat capacity, Wang et al. [184] proposed a model of a nanocrystalline compacted material in which all grains are rhombohedrons of the same size. The model unit cell consists of eight grains (Fig. 15). In modeling, the grain size d, which is defined as the diameter of a spherical particle with the same number

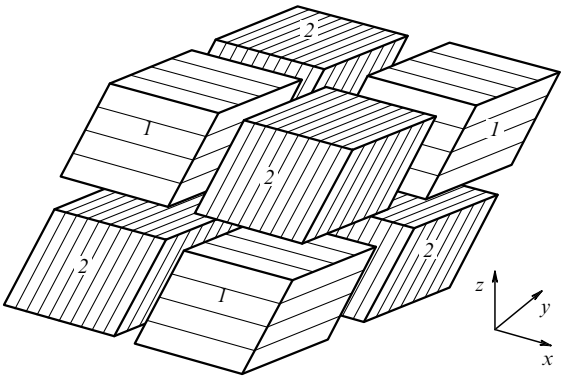

Figure 15. Three-dimensional model of the unit cell of a nanocrystal consisting of eight equal-size rhombohedral grains of types *1* and *2*; all faces of grains of the same type are crystallographically equivalent [184].

of atoms, was assumed to be 1.1, 2.0, and 2.8 nm. Interatomic interactions were described by the Lennard-Jones potential. Calculations of the density $g(\nu)$ of vibrational states revealed that, compared to the vibrational state density of an ideal fcc single crystal consisting of 500 atoms, $g(\nu)$ of the model nanocrystal ($d = 1.1$ nm) is smeared in the low- and high-frequency regions (Fig. 16). The majority of the additional low- and high-frequency vibrational modes are localized at the grain boundaries. According to such calculations, the nanocrystal has a higher heat capacity than the ideal fcc crystal, and the smaller the grains, the larger the difference ΔC in their heat capacities (Fig. 17). The anomalous excess heat capacity of the nanomaterial is primarily due to the low-frequency vibrational modes related to the grain boundaries. The contribution of high-frequency vibrations to the anomalous increase of the heat capacity of the nanocrystal is insignificant.

The internal energy and the excess heat capacity of nanocrystalline materials were also analyzed by Pirc and

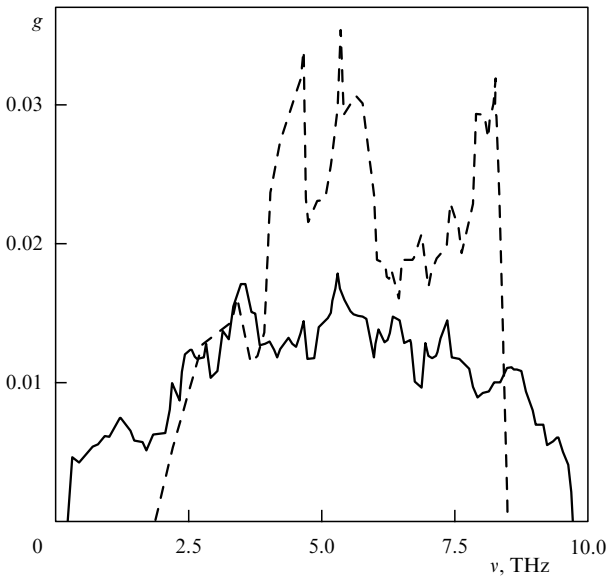

Figure 16. Density of vibrational states $g(\nu)$ for an ideal model compact nanocrystal whose grains have a diameter $d = 1.1$ nm (solid line) and for a defect-free fcc single crystal consisting of 500 atoms (dashed line) [184].

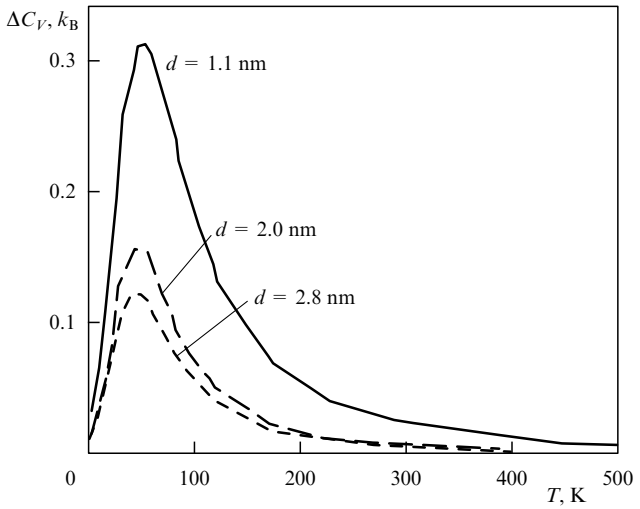

Figure 17. Dependence of the excess heat capacity ΔC_V on the temperature and grain size for a model compact nanocrystal [184].

Holz [185], who used a method equivalent to the mean-field approximation. According to them, in the low-temperature region the excess heat capacity ΔC is a linear function of the temperature.

In the simplest case, according to the Grüneisen relation, the thermal expansion coefficient α is proportional to the heat capacity C_V. Bearing this in mind, we can expect that nanocrystalline materials have higher values of α compared to those of ordinary polycrystals. Indeed, nc-Cu with an average grain size of 8 nm has $\alpha = 31 \times 10^{-6}$ K^{-1}, which is twice as large as the value $\alpha = 16 \times 10^{-6}$ K^{-1} for coarse-grained copper [2, 186].

To establish the effect of grain boundaries on the thermal expansion coefficient, Klam et al. [187] measured the thermal expansion of rolled copper foil with 17-μm grains and of polycrystalline copper with 19-mm grains. The thermal expansion coefficient of copper foil proved to be greater than that of coarse-grained copper. According to Klam et al. [187], the greater value of α in copper foil is due to the fact that the thermal expansion coefficient of grain boundaries is substantially larger than that of crystallites: for grain boundaries $\alpha_{gb} = (40-80) \times 10^{-6}$ K^{-1}, which is 2.5 to 5.0 times larger than the value of α for coarse-grained copper. Note that the copper foil studied by Klam et al. [187] is close in the production method to SMC materials, in which the atoms belonging to grain boundaries have an enhanced mobility.

Sui and Lu [188] studied the size dependence $\alpha(d)$ of the nanocrystalline alloy $Ni_{0.8}P_{0.2}$. Nanocrystalline samples with different grain sizes (ranging from 7.5 to 127 nm) were fabricated by crystallizing an amorphous alloy ribbon at different annealing temperatures, from 583 to 693 K. The measurements revealed that as the grain size decreases from 127 to 7.5 nm, the linear thermal expansion coefficient increases from $(15.5 \pm 1.0) \times 10^{-6}$ K^{-1} to $(20.7 \pm 1.5) \times 10^{-6}$ K^{-1} (Fig. 18). The linear thermal expansion coefficients of the coarse-grained Ni–P alloy ($d \geqslant 10$ μm) and of the amorphous Ni–P alloy are 13.7×10^{-6} and 14.2×10^{-6} K^{-1}, respectively. Sui and Lu [188] represented α_{nc} of the nanocrystal in the following form:

$$\alpha_{nc} = \alpha_{gb} f_{gb} + \alpha_g (1 - f_{gb}) , \qquad (14)$$

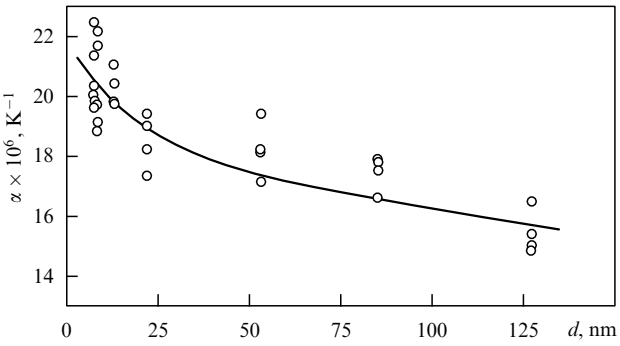

Figure 18. Linear thermal expansion coefficient α as a function of the grain size for the nanocrystalline alloy $Ni_{0.8}P_{0.2}$ [188].

where α_{gb} and α_g are the linear thermal expansion coefficients of the grain boundaries and the grains, respectively; $f_{gb} = c/d$ is the volume fraction of grain boundaries; $c = 1.9$ is a constant; and d is the grain size. Calculations using experimental data revealed that as d decreases, the difference $\alpha_{gb} - \alpha_g$ drops rapidly. For instance, at $d = 100$ nm $\alpha_{gb}/\alpha_g = 12.7$, i.e., the thermal expansion coefficient of the grain boundaries is ten times greater than that of the crystallites. For a nanocrystal with grains of several nanometers in diameter, $\alpha_{gb}/\alpha_g = 1.2$. Sui and Lu [188] believe that the substantial decrease in the difference $\alpha_{gb} - \alpha_g$ with decreasing grain size may be a consequence of densification of the grain boundaries or contraction of the nanometer-crystallite lattice. The latter seems a more likely reason.

The elevated heat capacity and the thermal expansion coefficient of nanocrystalline compacted materials suggest that such materials are thermodynamically unstable. Indeed, Weissmüller et al. [96], using nc-Pd as an example, found that the structural state of a nanocrystalline compacted material immediately after production is thermodynamically unstable (see Section 3.1).

The problem of thermodynamic stability of nanocrystalline compacted materials was studied by Gärtner et al. [189], who measured, at 613 K, the time dependence of the emf of high-purity nc-Pd with average grain sizes of 11 and 18 nm. For the reference electrode, they used coarse-grained palladium with grains of roughly 20 μm in diameter. They found that at 613 K the emf of the nanocrystalline samples was negative, grew rapidly during the first four to five minutes, and then increased slowly, asymptotically approaching zero. Because of the large area of the grain boundaries, the exchange electrochemical reaction in nc-Pd takes place at the grain boundaries at a high rate; in this case the emf E of the nanomaterial is directly linked to the thermodynamic characteristics of the grain boundaries through the following relation: $\Delta G_{gb} = -|z|FE$, where z is the valence of the palladium ion, F is the Faraday constant, and ΔG_{gb} is the Gibbs energy of the grain boundaries. Bearing this in mind, we conclude that a negative emf corresponds to a positive Gibbs energy of nanocrystalline palladium in comparison to coarse-grained palladium; this means that nc-Pd is thermodynamically unstable at elevated temperatures. According to Gärtner et al. [189], the rapid increase in the emf in the first stage of measurements is due to relaxation of the grain boundaries, while the stage in which the emf slowly approaches zero is due to grain growth. Similar behavior related to relaxation of the grain boundaries and grain growth was observed by Tschöpe et al. [190] in their calorimetric measurements involving nanocrystalline Pt. The emf after relaxation of the grain boundaries amounted to -36, -7 and -4 mV for Pt with grain sizes of 11, 18, and 20 nm, respectively. Thus, the smaller the grains, the lower the thermodynamic stability of the nanomaterial. The thermodynamic instability of a nanomaterial is determined primarily by the degree of nonequilibrium of the grain boundaries.

The results of measurement of the temperature dependence of the electrical conductivity of compacted nanomaterials are chiefly used to characterize the state of the grain boundaries and to determine the relaxation temperature.

The electrical resistivity ρ of nc-Cu ($d = 7$ nm) in the temperature range $0 < T \leqslant 275$ K is 20 times greater than for ordinary coarse-grained copper [191]. At $T \geqslant 100$ K, the values of the resistivity ρ of ordinary copper and nc-Cu increase linearly with temperature, but the temperature coefficient of resistivity for nc-Cu $\partial\rho/\partial T = 17 \times 10^{-9}$ Ω cm K^{-1} is larger than $\partial\rho/\partial T = 6.6 \times 10^{-9}$ Ω cm K^{-1} for ordinary copper. Analysis of the experimental dependence $\rho(T)$ for nanocrystalline and coarse-grained copper revealed that the electron scattering coefficient at the grain boundaries in nc-Cu is $r = 0.468$ at 100 K and 0.506 at 275 K, while for coarse-grained copper $r = 0.24$, which is lower by a factor of two. This difference is due to the different thickness and structure of grain boundaries in nanocrystalline and coarse-grained copper. The temperature behavior of r for nc-Cu can be explained by the large thermal expansion coefficient of the grain boundaries: according to [2, 180], $\alpha_{gb} = 66 \times 10^{-6}$ K^{-1}. Kai [191] believes that the elevated electrical resistivity ρ and temperature coefficient $\partial\rho/\partial T$ in nc-Cu are primarily due to electron scattering at grain boundaries. Another reason why the resistivity of nc-Cu is elevated may be the small mean free path λ of electrons: for nc-Cu $\lambda \approx 4.7$ nm, while for coarse-grained copper $\lambda \approx 44$ nm.

Investigations by Frolov et al. [192] of the resistivity of nanocrystalline cobalt films 2 to 50 nm thick demonstrated that ρ is almost temperature-independent, decreasing as the film becomes thicker, and is larger than ρ of bulk cobalt. They found that the large resistivity and the almost-zero temperature coefficient of resistance of nanocrystalline cobalt film are a consequence of the partial localization of electrons, when the grains become smaller than the electron mean free path. Localization affects the resistivity more strongly than the increase in the scattering of charge carriers by the grain boundaries, since the former reduces the concentration of charge carriers. As a result, a decrease in crystallite size leads to an increase in the degree of localization and a decrease in the concentration of charge carriers and, hence, to an increase in the electrical resistivity.

Islamgaliev et al. [193, 194] and Pekala and Pekala [195] measured the electrical resistivity of SMC copper, nickel, and iron prepared by equichannel corner extrusion. The average grain size in the SMC metals was 100 to 200 nm. At 80 K, the resistivity of SMC copper was almost two times higher than that of coarse-grained copper. The elevated resistivity of SMC copper is due to the higher coefficient r of electron scattering at the nonequilibrium grain boundaries. According to Mulyukov [196], the increase in r is due to the distortions of translational symmetry caused by long-range stress fields and the dynamically excited state of atoms in the interfacial phase. As a result of annealing at 420 – 470 K, there is a sharp drop in ρ, caused by the relaxation of the grain boundaries and their transition from a stressed nonequilibrium state to an equilibrium state. The slow reduction in ρ that follows the

annealing at $T > 470$ K is a consequence of grain growth and the weakening of electron scattering by grain boundaries.

4.3 Magnetic properties

The effect of the nanocrystalline state on the magnetic properties of paramagnets was studied by Rempel' et al. [70–73], who used palladium as an example. Conventional polycrystalline palladium with crystallites several microns in diameter possesses a unique electronic structure, which is extremely sensitive to ferromagnetic impurities or external pressure. This prompted Rempel' et al. [73] to assume that the formation of an SMC structure in palladium may affect the electronic structure and the magnetic susceptibility.

SMC palladium was produced from coarse-grained palladium by intense plastic deformation by applying torsion combined with quasihydrostatic pressure. Here, the true logarithmic degree of deformation $e = 7.0$ was reached. The density of SMC Pd coincided with that of the initial palladium and did not change after annealing at temperatures ranging from 300 to 1200 K. This suggests that SMC Pd is nonporous. The grain size in SMC Pd determined by electron-diffraction and electron-microscopy methods was 120–150 nm.

The magnetic susceptibility χ was measured by the Faraday method with an accuracy of $\pm 0.05 \times 10^{-6}$ emu g^{-1} in a 1.3×10^{-3} Pa vacuum (10^{-5} mm Hg). The magnetic susceptibility of the initial palladium and the SMC palladium was independent of the magnetic field strength H, which suggested that the samples had no ferromagnetic impurities. The temperature dependences were studied using two schemes. In the first one, the susceptibility was measured directly at the annealing temperature after holding at a temperature for 1 h; the corresponding dependences were denoted $\chi(T, T)$. In the second scheme, the susceptibility measurements were carried out at 300 K after a sample had been annealed at a temperature T and than cooled to room temperature; the corresponding dependences were designated $\chi(300, T)$. The results of the measurements for the initial (coarse-grained) and SMC palladium are given in Fig. 19 for the temperature range of 300–1225 K.

At $T < 825$ K, the susceptibility $\chi(300, T)$ of SMC Pd considerably exceeds the initial-palladium susceptibility, which is independent of the annealing temperature. Upon annealing at 825–1025 K, the susceptibility of SMC Pd first drops sharply and then decreases gradually to values of χ corresponding to the initial palladium. The temperature dependence $\chi(T, T)$ for SMC Pd (curve *2* in Fig. 19) exhibits no such rapid transition; as the temperature grows, the susceptibility of SMC Pd decreases gradually to finally coincide with the $\chi(T, T)$ curve for the initial palladium; starting from $T = 725$ K the temperature curves $\chi(T, T)$ for SMC Pd and the initial palladium are, for all practical purposes, the same.

The main contribution to the magnetic susceptibility of polycrystalline palladium is provided by Pauli's spin paramagnetism of conduction electrons, χ_P [197]. Here, there is a strong Stoner enhancement of χ_P (by a factor of 10 to 15) [198], which reflects the many-particle effects of electron interaction. Another important feature of palladium is the presence at the Fermi level of a high and narrow (approximately 0.3-eV wide) peak [198], which results in a high density of electron states at the Fermi level (roughly 2.3 states per electron volt per atom). The narrow peak in the density of states determines the sensitivity of the palladium properties to the position of the Fermi level.

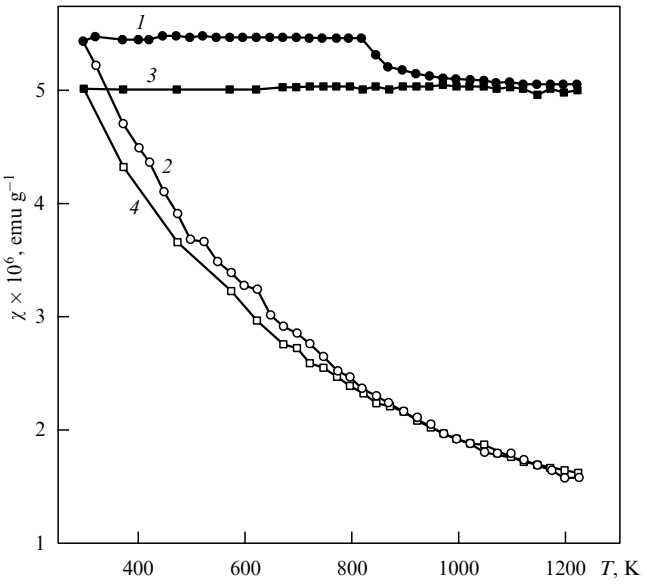

Figure 19. Magnetic susceptibilities χ of SMC and coarse-grained palladium: (*1*) and (*2*) SMC Pd, $\chi(300, T)$ and $\chi(T, T)$ curves, respectively; (*3*) and (*4*) coarse-grained Pd, $\chi(300, T)$ and $\chi(T, T)$ curves, respectively [71]. For designations, see text.

In the low-temperature region (below approximately 50 K) [199], the magnetic susceptibility of palladium increases in proportion to the square of the temperature and is described by the Pauli formula common for fermions:

$$\chi_P(T) = \chi_P(0)\left(1 + \frac{1}{6}\,\pi^2 v_0 k_B T^2\right), \qquad (15)$$

where $\chi_P(0)$ is the magnetic susceptibility at absolute zero with allowance for Stoner enhancement, and v_0 is a constant dependent on the density of states at the Fermi level $N(E_F)$ and also on its first and second energy derivatives.

As the temperature grows, the susceptibility of palladium passes through a pronounced maximum in the 50–100 K range and then rapidly falls off [199, 200]. Rempel' et al. [70–73] studied the high-temperature region ($T \geqslant 300$ K), in which the contribution (15) to the magnetic susceptibility gradually decreases and the experimental temperature curve $\chi(T)$ exhibits no maximum.

The statistical processing of the temperature curves of magnetic susceptibility, $\chi(T)$, measured by Rempel' et al. [70– 73] in the initial palladium and SMC Pd demonstrated that at $T \geqslant 775$ K the curves are adequately described by the Curie formula

$$\chi = \frac{C}{T} = \frac{1}{3}\,\frac{N_A}{\rho}\,\frac{\mu_B^2 p^2}{k_B T}, \qquad (16)$$

where χ is the magnetic susceptibility per unit mass, C is the Curie constant, N_A is Avogadro's number, μ_B is the Bohr magneton, ρ is the density of matter, and p is the effective number of Bohr magnetons per atom. For $T \geqslant 775$ K, the Curie constants C for the initial palladium and SMC Pd coincide within experimental error and are 1945 ± 10 emu K g^{-1}. The effective magnetic moment calculated by formula (16) with the above value of the Curie constant is $\mu_{eff} = p\mu_B = 0.44\mu_B$. The gradual and

continuous transition of the susceptibility from the Pauli relation to the Curie relation, observable over a broad temperature range from 50 to 775 K, a transition related to thermal excitation of electrons and a smearing of the Fermi level, can be considered as being similar to the transition in the distribution of electrons from Fermi – Dirac statistics to classical Maxwell – Boltzmann statistics. The susceptibility of Boltzmann electrons is not related to the density of states at the Fermi level; rather, it is due only to the fact that the localized magnetic moments of the electrons are uncompensated. For this reason, at high temperatures the magnetic susceptibility of palladium is insensitive to agents affecting the density of states. This conclusion is corroborated by the results of Rempel' et al. [70 – 73], who found that the temperature curves of susceptibility, $\chi(T)$, for the initial palladium and SMC-Pd coincide for $T > 775$ K.

The most interesting result of Rempel's et al. [70 – 73] is a considerable difference ($\sim 8\%$) observed (at 300 K) between the susceptibilities of SMC Pd and the initial coarse-grained palladium. This difference remains after SMC-Pd has been annealed at $T < 825$ K. Rempel' et al. [70, 71] infer that this difference in χ cannot be related to variations in the volume content of the grain boundaries and their transition from a stressed nonequilibrium state to an equilibrium state, since according to electron-microscopic data and the results of microhardness measurements (see Fig. 10) the greatest grain growth, the reduction of the dislocation density, and the relaxation of grain boundaries occur after annealing at temperature much lower than 800 K. In particular, the volume fraction of grain boundaries in SMC Pd as a result of annealing in the 30 – 810 K range changes by a factor of ten, while the density of lattice dislocations changes by a factor of 1000, but this has no effect on the behavior of the susceptibility, whose reduction begins only at an annealing temperature higher than 810 K (curve *1* in Fig. 19). Rempel' et al. [70 – 72] believe that the most likely type of defects affecting the behavior of the susceptibility is intragrain vacancy complexes. Schaefer et al. [106] found that in nanocrystalline n-Pd ($d = 5 – 10$ nm) the vacancies form clusters (complexes), which have a lower mobility than separate vacancies and continue to exist up to temperatures higher than 400 K. The effect of intragrain vacancy complexes on the magnetic susceptibility of SMC Pd may be a consequence of variations in the density of electron states at the Fermi level. As noted earlier, in palladium the Fermi level lies on the slope of a very narrow and high peak in the density of states $N(E)$ [198]. The introduction of c_v vacancies into the palladium lattice generates $n_e c_v$ states in the conduction band ($n_e = 10$ is the number of electrons in the conduction band per palladium atom). If, as a result of the injection of c_v vacancies, the energy of the Fermi level decreases by ΔE_v, the number of states released is

$$\int_{E_F - \Delta E_v}^{E_F} N(E)\,\mathrm{d}E = n_e c_v\,. \tag{17}$$

Using the numerical data of Mueller et al. [198] on $N(E_F)$, $N'(E_F)$, and $N''(E_F)$ and expanding $N(E)$ in a Taylor series to within second-order terms, the authors of [71] found that at absolute zero, for the susceptibility and, hence, the density of states at the Fermi level to increase by a factor of 1.08, the Fermi energy must decrease by $\Delta E_v = 0.014$ eV (in [70, 71], the value $\Delta E_v = 0.14$ eV is an error). Allowing for all this and using formula (17) reveals that the vacancy concentration that guarantees the required increase in $N(E_F)$ and decrease in the Fermi energy by $\Delta E_v = 0.014$ eV is 0.003 vacancy per atom. Such a vacancy concentration (0.3 at.%) can be attained without any difficulty by intense plastic deformation, since the formula given in [201]

$$c_v \approx \left[\exp(e) - 1\right] \times 10^{-4} \tag{18}$$

at $e = 7$ yields a much higher vacancy concentration.

At $T > 500$ K, the smearing of the Fermi level by $\sim k_B T$ becomes comparable to the width of the narrow peak in the density of states near the Fermi level, so that at high temperatures the effect of vacancies on the magnetic susceptibility of palladium is insignificant. This explains the absence of a jump in the temperature curve $\chi(T)$ for SMC Pd.

Thus, the elevated susceptibility of SMC Pd is related to the excess concentration of vacancies united into complexes. The return of the susceptibility of SMC Pd to the values of χ characteristic of coarse-grained palladium is caused by the condensation of vacancies and the annealing of dislocation tangles at $T > 825$ K. Additional confirmation of the conclusions of Rempel' et al. [70, 71] concerning the effect of vacancy complexes on the magnetic susceptibility of SMC palladium is provided by the study by Wurschum et al. [202] of positron lifetimes in this material.

According to Wurschum et al. [202], the spectrum of positron lifetimes in SMC Pd has strong (with an intensity of about 95%) and weak (with an intensity of $\sim 5\%$) components with corresponding lifetimes $\tau_1 \approx 167$ ps and $\tau_2 \approx 280 – 330$ ps. The value of τ_1 is characteristic of free volumes close to that of a lattice vacancy. The value of τ_2 is characteristic of positron annihilation in vacancy pores with volumes of 6 to 12 removed atoms. Vacancy complexes are observed in SMC Pd up to $T \simeq 455$ K. Thus, the positron-annihilation results of Wurschum et al. [202] have corroborated the assumption, made in [71], that there are vacancy complexes in SMC Pd at $T < 500$ K and that these complexes have a strong effect on the electron-energy spectrum of palladium near the Fermi level.

Rempel' et al. [68] studied the magnetic properties of SMC Cu prepared from coarse-grained diamagnetic copper by intense plastic deformation. The initial copper, which contained about 0.01 at.% dissolved iron, was diamagnetic over the entire temperature range (300 – 1225 K), and the $\chi(T, T)$ curve obtained for the initial copper is in good agreement with the data of Garber et al. [203]. As a result of intense plastic deformation of the initial copper by equichannel corner extrusion (the true logarithmic degree of deformation was 3.5), SMC n-Cu was produced with grains 130 – 150 nm in diameter and precipitation of iron particles earlier dissolved in the copper occurred. The magnetic measurements were made in a vacuum of 1.3×10^{-3} Pa (10^{-5} mm Hg) on a highly sensitive magnetic balance in a field with induction 8.8 kG at temperatures varied in steps of 25 K in the range of 300 to 1225 K.

We again, as when describing Fig. 19, will designate the curves of the temperature dependence of χ measured directly at the annealing temperature by $\chi(T, T)$ and those obtained in measurements of samples that were cooled to room temperature after annealing, by $\chi(300, T)$. The results are depicted in Fig. 20.

The measurements demonstrate that the susceptibility of SMC copper is much higher than the susceptibility of the initial copper. Moreover, the susceptibility of n-Cu becomes

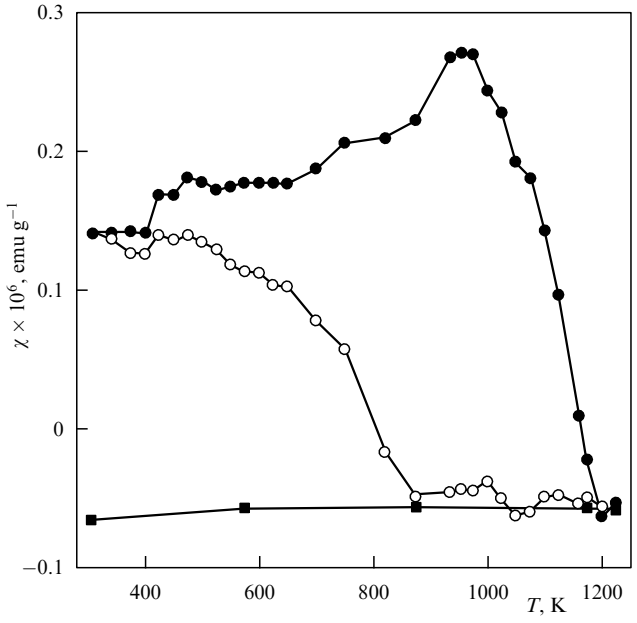

Figure 20. Magnetic susceptibility χ of a nanocrystalline copper matrix (n-Cu) with iron impurities, measured in a magnetic field with induction 8.8 kG [68]: (○) $\chi(T, T)$ dependence; (●) $\chi(300, T)$ dependence, and (■) cooling curve (corresponds to the susceptibility of copper with 0.01% iron dissolved in the copper).

inversely proportional to the magnetic field strength H, which is an indication that the sample contains a ferromagnetic impurity, iron. As is known (see [204]), dissolved iron precipitates from copper on rolling. Rempel' et al. [68] demonstrated that precipitation of iron particles that were dissolved in copper was initiated by intense plastic deformation.

In the $\chi(300, T)$ curve near the nanotransition temperature $T_n \approx 425$ K (the transition of copper from the SMC state to the coarse-grained state), a jump in susceptibility is observed. Then, in the temperature interval from 450 to 650 K, the susceptibility remains almost flat. Finally, as the temperature increases still further, there is a peak at 975 K and then a sharp drop to values corresponding to the susceptibility of diamagnetic copper (see Fig. 20). The susceptibility $\chi(300, T)$ ceases to depend on the magnetic field strength H after annealing at $T > 1200$ K.

The $\chi(T, T)$ dependence exhibits a slight decrease in χ at $T < 425$ K; after a slight increase in the temperature interval 425–475 K, the susceptibility drops to diamagnetic values, and at 850 K it coincides with the temperature curve for the susceptibility of conventional copper. The dependence of χ on the magnetic field strength H disappears at $T > 850$ K.

The curve of susceptibility measured upon cooling from 1225 down to 300 K (see Fig. 20) corresponds to the susceptibility of copper with 0.01 at.% of iron dissolved in the copper [205]. There is no dependence of susceptibility on the magnetic field strength.

One of the most interesting experimental facts discovered by Rempel' et al. [68] is the jump in both the $\chi(300, T)$ and $\chi(T, T)$ curves at a temperature $T_n \approx 425$ K corresponding to the transition from SMC to coarse-grained copper. Is this jump related to changes in the susceptibility of copper itself? The main contributions to the magnetic susceptibility of crystalline copper is the diamagnetism of atomic cores, Pauli's spin paramagnetism, and Landau's diamagnetism of conduction electrons. The sum of these contributions for copper is negative, with the result that copper is diamagnetic. The weak quadratic temperature dependence of susceptibility [203] is caused by the Pauli's contribution. In the case at hand, the susceptibility of n-Cu is positive because of the precipitation of iron particles. The lower susceptibility of SMC copper (the $\chi(300, T)$ curve in Fig. 20) may be the result of the smaller density of states at the Fermi level and the smaller effective mass of the conduction electrons. But, still, this cannot lead to a sharp drop of the temperature curve. For this reason, it is impossible to explain the difference in the susceptibility values in the $\chi(300, T)$ and $\chi(T, T)$ curves for n-Cu after the nanotransition has taken place ($\Delta\chi = \chi(300, T) - \chi(T, T)$ at $T \approx 500$ K) only by changes in the state of copper.

The analysis made by Rempel' et al. [68] shows that the jump in χ in these curves at 425–450 K is most likely related not to changes in copper susceptibility but to changes in the magnetic contribution of the iron impurities that precipitate in the form of nanoparticles at the copper grain junctions.

If we assume that the jump in susceptibility in the $\chi(300, T)$ and $\chi(T, T)$ curves upon the nanotransition to n-Cu is related to changes in the magnetic contribution of impurities, then we can subtract the copper susceptibility $\chi_{Cu}(T)$ from $\chi(T)$ and determine the contribution of the ferromagnetic phase $\chi_{Fe}(T)$ to the susceptibility (Fig. 21). This phase may be either a surface phase or a volume phase. In the first case (a two-dimensional ferromagnetic phase), it could lie in the boundary between two grains, and if the phase is three-dimensional, it is most likely to be found at the junctions of three or more grains. Let us discuss in greater detail the approximation of $\chi_{Fe}(T)$ made by Rempel' et al. [68]. The assumption was that the precipitated iron particles have the same size and that the Curie point T_C of iron is independent of the nanoparticle size.

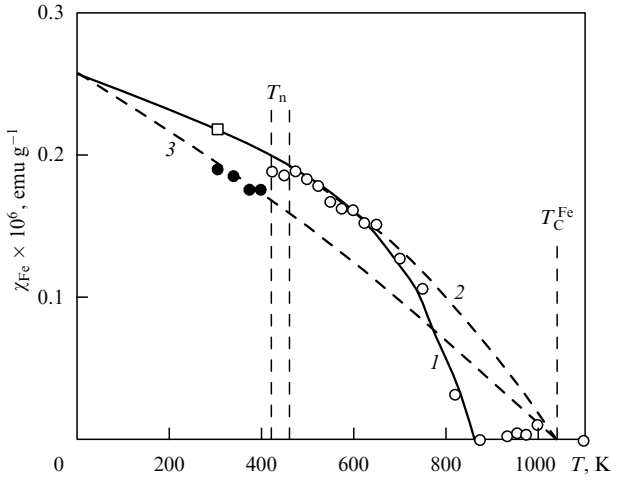

Figure 21. Approximation of the temperature dependence of the susceptibility of an impurity superparamagnetic phase [68]: curves *1* and *2* represent the variations in the susceptibility after the nanotransition with and without allowance for dissolution of iron impurities, curve *3* represents the variation of susceptibility prior to the nanotransition, and □ is the value of the susceptibility of the superparamagnetic impurity at 300 K after the nanotransition in copper has been completed. The vertical dashed lines limit the region of the nanotransition near the temperature T_n and the Curie point of iron T_C^{Fe}.

The temperature dependence of the susceptibility in saturation magnetic fields at low temperatures for ordinary ferromagnets is not as strong as that observed experimentally (see Fig. 21) [68]. A strong dependence at low temperatures is possible if the precipitating iron particles are superparamagnetic. The superparamagnetic contribution χ_{sp}, expressed in dimensionless units, at a temperature T in a magnetic field H can be expressed in the following form [206]:

$$\chi_{sp} = n_{sp} V_{sp} \frac{M_s(T)}{H} L\left(\frac{V_{sp} M_s(T) H}{k_B T}\right), \tag{19}$$

where $L = \coth(x) - 1/x$ is the Langevin function, n_{sp} is the number of superparamagnetic particles per unit volume, V_{sp} is the volume occupied by a superparamagnetic particle, and $M_s(T)$ is the saturation magnetization of the ferromagnetic phase at temperature T.

The temperature dependence of the saturation magnetization of the crystalline ferromagnetic phase, $M_s(T)$, can be found by solving the equation

$$\frac{M_s(T)}{M_s(0)} = \tanh \frac{M_s(T) T_C}{M_s(0) T}, \tag{20}$$

where $M_s(0)$ is the saturation magnetization at $T = 0$ K. For crystalline iron, $M_s(0) = 1740$ G and $T_C = 1043$ K [207]. The saturation magnetization $M_s(0) = 1740$ G corresponds to a magnetic moment of iron atoms of $2.22\,\mu_B$ (μ_B is the Bohr magneton).

The ferromagnetic contribution disappears at 850 K, which is much lower than the Curie point of ordinary polycrystalline iron (see Fig. 21). This can be related to total dissolution of the ferromagnetic impurity in copper already at 850 K. According to the phase diagram [204], the concentration of the undissolved iron, $c_{Fe}(T)$, in copper lowers with increasing temperature as follows:

$$c_{Fe}(T) = c_{Fe}(0) - C \exp\left(-\frac{E_m}{k_B T}\right), \tag{21}$$

where $c_{Fe}(0) \approx c_{Fe}(300)$ is the relative atomic concentration of iron in the form of a ferromagnetic phase at absolute zero or a practically equal concentration at 300 K, C is a constant, and E_m is the mixing energy. According to Tammann and Oelsen [204], $C = 43$ and $E_m/k_B = 9217$ K, or $E_m = 0.79$ eV.

To pass from the dimensionless volume susceptibility χ_{sp} and atomic concentration c_{Fe} to the mass susceptibility of the ferromagnetic phase, whose concentration changes as a result of dissolution, we can use the following relation:

$$\chi_{Fe}(T) = \chi_{sp}(T, n_{sp}, V_{sp})\, c_{Fe}(T) \frac{A_{Fe}}{A_{Cu}\rho_{Fe}}, \tag{22}$$

where $A_{Cu} = 63.55$ and $A_{Fe} = 55.85$ are the atomic weights of copper and iron, respectively, and $\rho_{Fe} = 7.86$ g cm^{-3} is the iron density. Approximating the temperature dependence of susceptibility, $\chi_{Fe}(T)$, in the 425 – 1043 K range by Eqn (22), allowing for (19) – (22), and setting the Curie point to 1043 K and the mixing energy to 0.79 eV, Rempel' et al. [68] obtained good agreement with the experimental results (curve *1* in Fig. 21). Curve 1 passes also at 300 K through the point denoted by □, which corresponds to the values of $\chi(300, T)$ in the range of annealing temperatures 450 – 600 K and would land on the $\chi(T, T)$ curve if not for the jump in susceptibility upon the nanotransition in copper. Curve *2* in Fig. 21 has been constructed without allowance for the dissolution of iron, i.e., for a constant concentration of the ferromagnetic impurity up to the Curie point. The approximation (curve *1* in Fig. 21) yields $V_{sp} = 1.8 \times 10^{-20}$ cm^3 for the volume occupied by a superparamagnetic particle and $n_{sp} = 5.7 \times 10^{14}$ cm^{-3} for the number of such particles after nanotransition, and also the value of the constant, $C = 0.4$. The value of C is approximately a hundred times smaller than the value given by Tammann and Oelsen [204]. The higher rate of iron dissolution (compared to that observed under equilibrium conditions) is the consequence of the fact that the precipitation of iron nanoparticles and their existence in the copper matrix are thermodynamically nonequilibrium processes.

If we ignore the dissolution of iron in copper up to 650 K, the relative volume concentrations of the superparamagnetic impurity, $n_{sp}V_{sp}$, in copper before and after the nanotransition are equal. Hence, in accordance with (19), the superparamagnetic contributions at absolute zero are equal, too. Assuming that the Curie point is independent of the size of the superparamagnetic particles and that the copper susceptibility does not change as a result of the nanotransition, we can approximate the experimental data for the susceptibility prior to the nanotransition (curve *3* in Fig. 21). This approximation shows that prior to the nanotransition the volume occupied by the superparamagnetic particles was 1.62 times smaller and the average particle size was $(1.62)^{1/3} = 1.17$ times smaller than after the transition. The difference in the temperature curves for the susceptibility before and after the transition is related to the increase in the average size of superparamagnetic nanoparticles from 2.8 to 3.3 nm.

A single superparamagnetic impurity particle occupies a volume $V = 1/n_{sp}$ in the copper matrix, which means that we can find the linear size corresponding to this volume. It turns out that for each superparamagnetic particle there is a copper particle 128 nm in diameter before the nanotransition and 150 nm after. These sizes coincide, in order of magnitude, with those of copper grains in the sample before and after the transition, which means that we can assume that the impurity particles are distributed uniformly in copper and that a single iron particle corresponds to each copper grain. This iron particle can be at a junction, i.e., a point where several grains meet. As the copper grains become larger in the process of the transition from the SMC state to the coarse-grained state, the number of grain junctions decreases and the atoms of the iron impurity are forced to diffuse along the surface of the copper grains to the remaining junctions. Here the remaining impurity nanoparticles become larger and their number drops. Similar processes also take place at higher annealing temperatures, when the growth of copper grains continues.

In the temperature range 450 to 600 K, the $\chi(300, T)$ dependence (see Fig. 20) is virtually constant. This means that the state of the superparamagnetic impurity, i.e., the number and size of particles, does not change on heating followed by cooling in this temperature range. For the $\chi(T, T)$ dependence, this is corroborated by calculation (curves *1* and *2* in Fig. 21), which indicates that the dissolution of iron at 450 – 600 K is negligible. The increase in the $\chi(300, T)$ susceptibility by approximately $\sim 1 \times 10^{-7}$ emu g^{-1} observed after annealing at temperatures from 650 to 975 K (see Fig. 20) is partially related to the increase in the size of superparamagnetic particles in the copper cooled to 300 K and, consequently, to the increase in the impurity contribution at 300 K. However,

this can explain an increase in $\chi(300, T)$ by only $\sim 2 \times 10^{-8}$ emu g^{-1}. The remaining portion is related to other factors, such as the smaller saturation magnetization M_s of the nanoparticles compared to the value for a bulk crystal, or the precipitation of a large amount of the ferromagnetic phase in the process of cooling.

According to Rempel' et al. [68], a reduction of susceptibility in the 1000 to 1225 K range is only observed when the rate at which the sample is cooled is high, i.e., in quenching the high-temperature states, when the entire ferromagnetic impurity remains dissolved in the copper. If, after annealing, the sample cools off slowly, the iron impurity has time to precipitate into the ferromagnetic phase and the decrease in the $\chi(300, T)$ susceptibility after the maximum, which is the case illustrated by Fig. 20, is absent.

Most studies of the magnetic properties of nanocrystalline compact materials involve ferromagnetic metals and alloys.

The saturation magnetization I_s, the Curie point T_C, and the coercive force H_c of nanocrystalline compacted nc-Ni ($d = 10$ nm) and single-crystal nickel were studied by Schaefer et al. [91]. The magnetic measurements were carried out in the 5 to 680 K temperature range in a magnetic field of up to 5.5 T. At $T < 300$ K, the magnetization of nc-Ni was smaller than the value of I_s for the single crystal. Measurements of the temperature dependence of the magnetization of nc-Ni in a 0.017-T field revealed that at a temperature ranging from 510 to 545 K the magnetization decreases sharply (by about 20%). Schaefer et al. [91] assumed that this reduction is related to a ferromagnetic – paramagnetic transition of the matter in the grain boundaries and, therefore, the Curie point for the grain-boundary phase of nc-Ni is $T_C = 545$ K. Further heating nc-Ni, accompanied by grain growth from 15 to 48 nm, results in a decrease and complete vanishing of the magnetization at a Curie point of 630 K, which corresponds to T_C of coarse-grained nickel. When the sample is cooled from 650 to 450 K, the transition into the ferromagnetic state occurs at 630 K, and after that the magnetization slowly increases without any features; the values of magnetization upon cooling are higher than upon heating of nc-Ni. According to Schaefer et al. [91], at absolute zero the magnetization of nc-Ni amounts to $0.52\,\mu_B$ per atom, in contrast to the value for coarse-grained nickel, for which $I_s(0) = 0.6\mu_B$ per atom. The coercive force H_c of nc-Ni in the 100 to 300 K range did not change and amounted to ~ 10 Oe. The most unusual result obtained by Schaefer et al. [91] is the lowering of the Curie point of nc-Ni, so that later Kisker et al. [208] again studied the magnetic properties of nc-Ni, this time focusing, however, on oxygen as the impurity. They found that the unusual reduction of the magnetization of nc-Ni at 510 – 545 K observed earlier is due to the presence of oxygen impurity, so that it is unjustified to speak of a change in the Curie point of nanocrystalline nickel. Indeed, a rough estimate shows that each impurity oxygen atom lowers the total ferromagnetism by a quantity corresponding to the contribution from a single nickel atom [191].

Valiev et al. [77] reported a reduction in T_C for nc-Ni ($d = 70 – 100$ nm) by 30 – 40 K in comparison to the value for ordinary coarse-grained nickel. The result was obtain by scanning calorimetry and by measuring the temperature dependence of the saturation magnetization. Measurements of $I_s(T)$ revealed that at 300 K the magnetization of nc-Ni ($d = 100$ nm) is roughly 10% smaller than the value of I_s for coarse-grained ($d \approx 1$ μm) nickel. Compact samples of nc-Ni were produced by Valiev et al. [77] by pressing the nanopowder in air, which means that the samples contained a lot of oxygen. Allowing for the high sensitivity of the magnetic properties of nickel to an impurity of oxygen [209] and taking into account the results of Kisker et al. [208], we can assume that the effects observed by Valiev et al. [77] are not directly related to the nanostate of nickel; rather it is a consequence of the nanocrystalline nickel being contaminated by oxygen.

A small ($\sim 3\%$) decrease in the magnetization of SMC Ni produced by torsion under quasihydrostatic pressure was reported by Korolev et al. [210]. The size of the SMC-Ni grains was assumed to be 100 – 200 nm. The temperature-dependence curves $\chi(T)$ for the susceptibility of SMC-Ni samples had a shape characteristic of ferromagnets. On initial heating of a plastically deformed sample of SMC Ni, the lowering of the susceptibility as the temperature approached the Curie point proceeded smoothly, while in thoroughly annealed samples of SMC Ni, a sudden drop in χ was observed as the temperature approached T_C (a similar drop was observed for undeformed nickel near the ferromagnet – paramagnet transition point). As a result of a series of annealing processes, the susceptibility of deformed nickel was found to increase up to values of χ corresponding to the initial nickel. Korolev et al. [210] attribute the observed anomalies in the magnetic properties of SMC Ni to the fact that the finest crystallites of SMC Ni are in a superparamagnetic state. In this case, SMC Ni must be interpreted as a heterogeneous material whose magnetic susceptibility is a linear combination of the susceptibilities of ferromagnetic and superparamagnetic components.

The validity of the explanation given by Korolev et al. [210] is questionable, since they assume that the grain boundaries are in an amorphous state and form a paramagnetic shell surrounding each Ni grain, thus effectively isolating the grains from each other. However, contemporary experimental data indicate that, even in the materials with smaller grains, the grain boundaries retain their crystal structure (see Section 3). Moreover, amorphous nickel is in a paramagnetic state only at $T > 530$ K and can hardly be considered a good magnetic insulator with an average grain boundary thickness of 3 nm. The superparamagnetic behavior of nickel can be observed when the particles are smaller than 10 – 15 nm [211]. In SMC Ni with an average grain size greater than 100 nm, the fraction of grains with $d < 10$ nm is negligible. Kisker et al. [208] found that after nanocrystalline nickel containing oxygen as an impurity is annealed, its magnetization increases. Comparison of the results of Kisker et al. [208] with those of Korolev et al. [210], which were concerned with the nature of the variation of χ of SMC Ni after several consecutive annealing processes, suggests that the effects observed by Korolev et al. [210] are related to the presence of oxygen in SMC Ni as an impurity. Contamination of nickel by oxygen could have occurred during the plastic deformation, which was done in air.

The study of the temperature dependence of the coercive force H_c of nickel – copper alloys made by Korolev et al. [212] demonstrated that intense plastic deformation has no effect on the Curie point of nickel, while the coercive force H_c of the SMC Ni – Cu alloy and SMC Ni is several times stronger than those of the initial alloy and coarse-grained nickel.

The research by Mulyukov et al. [79, 80] of the microstructure and magnetic hysteresis of SMC nickel and cobalt corroborate the fact that the coercive force of plastically deformed ferromagnets is several times stronger than that of the initial metals. Mulyukov et al. [79] found that the

annealing of SMC Ni at $T \leqslant 470$ K weakens the coercive force, with the grain size remaining practically unchanged. Annealing at higher temperatures is accompanied by a reduction in H_c and an increase in grain size. This implies that the elevated coercive force of SMC metals and alloys is due equally to the stressed nonequilibrium state of grain boundaries, on the one hand, and to small grain size, on the other. Relaxation of grain boundaries as a result of annealing or grain growth reduces H_c.

Hirscher et al. [213] used the magnetic aftereffect and magnetic saturation methods to study the structure of grain boundaries in nc-Fe ($d = 10-15$ nm). The magnetic aftereffect method amounts to finding the time dependence of the magnetic susceptibility after demagnetizing. The annealing of nc-Fe at $T = 350-500$ K resulted in irreversible changes in the magnetic aftereffect spectrum; simultaneously, the time dependence of the magnetic aftereffect was observed. According to Hirscher et al. [213], such changes are caused by the reorientation of the atoms related to the decrease in the free volumes in the grain boundaries. After annealing nc-Fe at 600 K, the magnetic moment per iron atom at 5 K increased from $2.0\,\mu_B$ to $2.2\,\mu_B$, i.e., to the value corresponding to ordinary coarse-grained α-Fe. This means that in nc-Fe the local distribution of atoms in grain boundaries differs somewhat from the distribution in coarse-grained iron.

In the last decade, ferromagnetic amorphous alloys (metallic glasses) based on Fe with additions of Nb, Cu, Si, and B and based on Co or Fe–Co with additions of Si and B have drawn a lot of interest. Crystallization of such amorphous materials produces nanocrystalline alloys with grain sizes ranging from 8 to 20 nm. Such alloys possess exceptional magnetic properties. The nanocrystalline alloys Fe–Cu–Nb–Si–B ($Fe_{73.5}Cu_1Nb_3Si_{13.5}B_9$) came to be known as FINEMETs, which are soft-magnetic materials with a very weak coercive force, comparable to that of cobalt-based amorphous alloys, and a high magnetic saturation, close to that for iron-based amorphous alloys [58, 214].

The development of a nanostructure in an amorphous alloy presupposes a combination of a high rate of formation of crystallization centers and a low rate of growth of such centers. The presence of copper in Fe–Cu–Nb–Si–B increases the number of crystallization centers and favors their uniform distribution over the volume; Nb hinders the growth of grains; and Si facilitates the formation of the bcc α-Fe(Si) phase. The annealing of the amorphous alloy at 740–820 K makes possible the precipitation of crystallites of an ordered solid solution α-Fe(Si) 10 to 15 nm in diameter with an Si content of up to 13–19 at.%; the α-Fe(Si) crystallites are separated by a thin layer of the amorphous phase (Fig. 22) [214, 215]. The presence of copper lowers the activation energy for crystallization and facilitates the nucleation of the bcc α-Fe(Si) phase [216]. Crystallization at a higher annealing temperature leads to the formation of boride phases. The precipitation of one or another phase depends on the relation between the annealing temperature and time: the amount of the bcc phase grows and that of the amorphous phase decreases as the annealing temperature and time increase. The highest magnetic permeability μ and the largest magnetic saturation is observed in alloys with a high content of the bcc phase, prepared by annealing at 780–820 K for one hour.

In ordinary ferromagnetic alloys, grain growth decreases the coercive force. According to Yamauchi and Yoshizawa [214], for nanocrystalline alloys of the Fe–Cu–*M*–Si–B systems (*M* is Nb, Ta, W, Mo, Zr, or V) the coercive force is proportional to the square of the grain size, i.e., $H_c \sim d^2$. The $Fe_{73.5}Cu_1Nb_3Si_{13.5}B_9$ alloy with an average grain size of about 10 nm has an extremely small coercive force $H_c \approx 0.5$ A m^{-1}. The high sensitivity of the magnetic permeability, coercive force, saturation magnetization, magnetostriction, and other magnetic characteristics of these alloys to the alloy microstructure stimulated an intensive research into the conditions of crystallization of amorphous alloys [215–226].

Noskova et al. [221, 227] demonstrated that preliminary deformation ($\sim 6\%$) of a ribbon of the amorphous alloy $Fe_{73.5}Cu_1Nb_3Si_{13.5}B_9$ by rolling and subsequent annealing for one hour at 813–820 K produces an additional decrease in grain size from 8–10 nm to 4–6 nm. Low-temperature annealing of the alloy at 723 K for one hour and subsequent short-duration annealing at 923 K (for ten seconds) produced a nanocrystalline structure with a grain size of 4–5 nm. The phase composition of the alloys produced by these methods was the same as after ordinary crystallization at 810–820 K.

Other soft-magnetic nanocrystalline alloys produced by crystallizing amorphous alloys are also known. The Fe–*M*–C, Fe–*M*–B, Fe–*M*–N, Fe–*M*–O (*M* is Zr, Hf, Nb, Ta, or Ti) alloys (see Fig. 22) with an average grain size of 10 nm have saturation magnetizations of 1.5–1.7 T, permeabilities $\mu = 4000-5000$, and small ($< 10^{-6}$) magnetostrictions [214, 228–230].

The crystallization of amorphous alloys makes possible not only the production of soft-magnetic materials but also

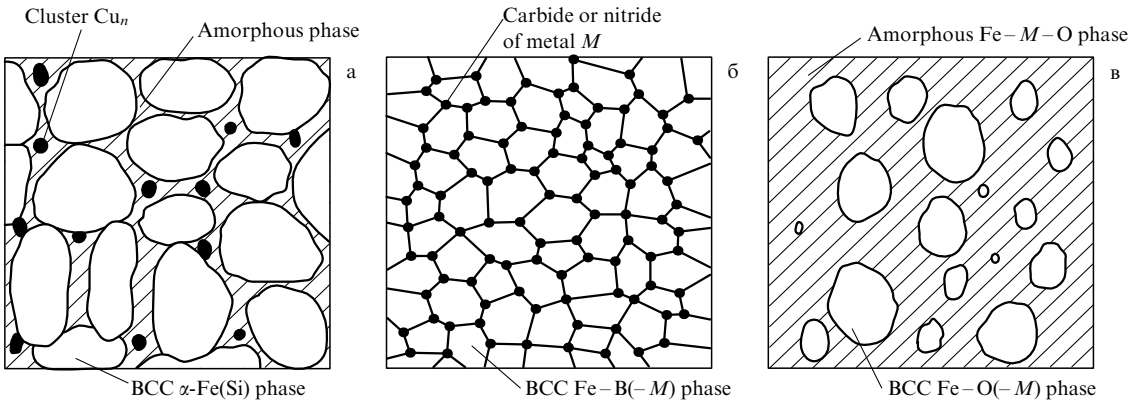

Figure 22. Schematic of the microstructure of typical nanocrystalline soft-magnetic alloys produced by crystallization from the amorphous state [214].

hard-magnetic materials with a high coercive force. Noskova et al. [231] demonstrated that annealing the amorphous soft-magnetic ($H_c \leqslant 40$ A m^{-1}) alloys $Fe_{81}Si_7B_{12}$ and $Fe_{60}Cr_{18}Ni_7Si_xB_{15-x}$ ($x = 3$ or 5) for one hour at 823 K increases H_c by a factor of 125 to 700. The rapid crystallization for ten seconds at 923 K of the amorphous soft-magnetic alloy $Fe_5Co_{70}Si_{15}B_{10}$ with $H_c \approx 1$ A m^{-1} makes it possible to produce a nanocrystalline alloy with an average grain size of 15 – 50 nm, $H_c = 8800$ A m^{-1}, and an elevated residual magnetization; a slowly crystallized alloy of the same composition has $H_c = 3000$ A m^{-1} [232, 233]. The high-coercivity state of the alloy produced by rapid crystallization is thermally stable and remains unchanged after annealing at 673 K. According to Glazer et al. [232] and Noskova et al. [233], the high value of the coercive force of a rapidly crystallized alloy compared to that of a slowly crystallized alloy is a consequence of the precipitation of anisotropic single-domain bcc particles of α-Fe with a high saturation magnetization, on the one hand, and the decrease in the grain size of α-Co, on the other. The increase in the residual magnetization of the nanocrystalline alloy could be caused by an exchange interaction between the magnetizations of grains that are smaller than the thickness of the interdomain boundary.

5. Conclusions

The studies conducted over the last decade have broadened our ideas about effects associated with the size of grains (crystallites) of solids. For a long time attention was focused on studying small particles, nanoclusters, whose properties are intermediate between those of single atoms and those of a polycrystalline solid. The development of methods of fabricating compact materials with exceptionally fine grain structures, where the grains have nanometer dimensions, made it possible to study the structure and properties of solids in the nanocrystalline state. At present, the main methods of preparation of nanocrystalline compact materials as the follows: compacting isolated nanoclusters prepared by evaporation and condensation, deposition from solutions, or decomposition of precursors; crystallization of amorphous alloys; and intense plastic deformation [1 – 5, 26, 32, 58, 63, 65, 86, 121, 214, 220].

Studies of the structure and properties of nanomaterials have developed very fast: the 1st International Conference on Nanostructured Materials was held in Mexico in 1993, and in 1995 – 1996, 26 international conferences were held on the same topic. From 1992, several new international scientific journals devoted exclusively to the nanocrystalline state have appeared.

An analysis of the experimental data gathered over the years shows that not only the grain size plays an important role in a nanocrystalline solid (just as it does in isolated nanoparticles) but so does the structure and the state of grain boundaries. Most vividly the effect of grain boundaries on the structure and properties manifests itself in nanomaterials prepared by compaction or intense plastic deformation. In such nanomaterials, immediately after their preparation, the grain boundaries are in a nonequilibrium stressed state with excess energy. Relaxation of the nonequilibrium grain boundaries in nanocrystalline metals and allows may occur spontaneously even at room temperature and is usually accompanied by grain growth [65, 96]. Ceramic (oxide) nanomaterials are more stable than metallic nanomaterials; the structure and the grain size of the former remain almost unchanged even after annealing at 600 – 800 K [98].

The properties of nanocrystalline metals and alloys, particularly of those produced by the compaction of nanoclusters, are very sensitive to oxygen as an impurity. The extremely large area of grain boundaries is responsible for the high chemical activity of nanocrystalline metals. A considerable fraction of the amazing results obtained before 1992, after being thoroughly checked, were found to be a consequence of contamination of the nanocrystalline materials by impurity oxygen, and in the case of palladium even by hydrogen.

In order to theoretically interpret the experimental data on nanocrystalline compact materials, the separation of surface (i.e., related to grain boundaries) and volume (i.e., related to grain size) effects is important. This problem has yet to be solved in full. On the whole, the level of theoretical treatment of these aspects and explanation of the structure and properties of compact nanocrystalline materials is much lower than in the case of isolated nanoparticles.

Analyzing the state of research in materials science, Academician N P Lyakishev formulated four stages in the 'life' of structural materials: the appearance of an idea, intensive studies, production growth, and production decline [234]. He believes that the development of compact nanocrystalline materials is in the second stage. In the immediate future, we will be witnesses to a rapid increase in the number of studies on compact nanomaterials. The most promising directions of research are, apparently, the detailed study of the microstructure; the separation of effects caused by grain size and grain boundaries; determining the conditions needed for the stabilization of the nanocrystalline structure, conditions guaranteeing that the properties will be retained; and the invention of new models of the nanocrystalline state, models that will make it possible to attain a level of theoretical description that correctly reflects reality.

The author is grateful to Prof. H-E Schaefer (Institute of Theoretical and Applied Physics, Stuttgart University, Germany) for providing the materials of the 2nd International Conference on Nanostructures (Stuttgart, 1995) and to the author's closest colleague Dr. A A Rempel' for fruitful discussions.

References

1. Gleiter H *Nanostruct. Mater.* **1** (1) 1 (1992)
2. Birringer R, Gleiter H, in *Encyclopedia of Material Science and Engineering*. Suppl. Vol. 1 (Ed. R W Cahn) (Oxford: Pergamon Press, 1988) p. 339
3. Siegel R W *Ann. Rev. Mater. Sci.* **21** 559 (1991)
4. Siegel R W *Nanostruct. Mater.* **3** (1 – 6) 1 (1993)
5. Schaefer H-E, in *Mechanical Properties and Deformation Behavior of Materials Having Ultrafine Microstructure* (Ed. M A Nastasi) (Dordrecht: Kluwer Academic Press, 1993) p. 81
6. Siegel R W *J. Phys. Chem. Solids* **55** (10) 1097 (1994)
7. Morokhov I D, Trusov L I, Chizhik S P *Ul'tradispersnye Metallicheskie Sredy* (Ultradisperse Metallic Media) (Moscow: Atomizdat, 1977)
8. Morokhov I D et al. *Usp. Fiz. Nauk* **133** (4) 653 (1981) [*Sov. Phys. Usp.* **24** (4) 295 (1981)]
9. Morokhov I D, Trusov L I, Lapovok V N *Fizicheskie Yavleniya v Ul'tradispersnykh Sredakh* (Physical Phenomena in Ultradisperse Media) (Moscow: Energoatomizdat, 1984)
10. Petrov Yu I *Fizika Malykh Chastits* (The Physics of Small Particles) (Moscow: Nauka, 1982)
11. Petrov Yu I *Klastery i Malye Chastitsy* (Clusters and Small Particles) (Moscow: Nauka, 1986)

12. Larikov L N *Metallofizika* **14** (7) 3 (1992)
13. Larikov L N *Metallofiz. Noveishie Tekhnol.* **17** (1) 3 (1995); **17** (9) 56 (1995)
14. Andrievskii R A *Usp. Khim.* **63** (5) 431 (1994)
15. Gen M Ya, Petrov Yu I *Usp. Khim.* **38** (12) 2249 (1969)
16. Smirnov B M *Usp. Fiz. Nauk* **162** (1) 119 (1992) [*Sov. Phys. Usp.* **35** (1) 37 (1992)]
17. Nepiiko S A *Fizicheskie Svoistva Malykh Metallicheskikh Chastits* (Physical Properties of Small Metallic Particles) (Kiev: Naukova Dumka, 1985)
18. Bohren C, Huffman D *Absorption and Scattering of Light by Small Particles* (New York: Wiley, 1983)
19. Perenboom J, Wyder P, Meier F *Phys. Rep.* **78** (2) 173 (1981)
20. Halperin W *Rev. Mod. Phys.* **58** (3) 533 (1986)
21. Nagaev E L *Usp. Fiz. Nauk* **162** (9) 47 (1992) [*Sov. Phys. Usp.* **35** (9) 747 (1992)]
22. Gleiter H, in: *Deformation of Polycrystals: Mechanisms and Microstructures* (Eds N Hansen et al.) (Roskilde: Risö Nat. Laboratory, 1981) p. 15
23. Gleiter H, Marquardt P *Z. Metallkd.* **75** (4) 263 (1984)
24. Birringer R, Herr U, Gleiter H *Trans. Jpn. Inst. Met. Suppl.* **27** 43 (1986)
25. Siegel R W, Hahn H, in: *Current Trends in Physics of Materials* (Ed M Yussouff) (Singapore: World Scientific, 1987) p. 403
26. Gleiter H *Prog. Mater. Sci.* **33** (4) 233 (1989)
27. Andrievskii R A *Poroshkovaya Materialovedenie* (Powder Materials Science) (Moscow: Metallurgiya, 1991)
28. Matthews M D, Pechenik A *J. Am. Ceram. Soc.* **74** (7) 1547 (1991)
29. Chen D-J, Maya M J *Nanostruct. Mater.* **2** (3) 469 (1992)
30. Andrievski R A et al. *Nanostruct. Mater.* **6** (1 – 4) 353 (1995)
31. Rabe T, Wäsche R *Nanostruct. Mater.* **6** (1 – 4) 357 (1995)
32. Kear B H, Strutt P R *Nanostruct. Mater.* **6** (1 – 4) 227 (1995)
33. McCandlish L E, Kear B H, Kim B K *Nanostruct. Mater.* **1** (1) 119 (1992)
34. Wu L et al., in: *Proc. of the 13th Intern. Plansee Seminar* (Eds H Bildstein and R Eck) (Reutte: Metallwerk Plansee, 1993) Vol. 3, p. 667
35. Fang Z, Eason J W, in: *Proc. of the 13th Intern. Plansee Seminar* (Eds H Bildstein and R Eck) (Reutte: Metallwerk Plansee, 1993) Vol. 3, p. 625
36. Seegopaul P, McCandlish L E, Shinneman F M *Int. J. Refr. Met. Hard Mater.* **15** (1 – 3) 133 (1997)
37. Ivanov V V et al. *Dokl. Akad. Nauk SSSR* **275** (4) 873 (1984) [*Sov. Phys. Dokl.* **29** (4) 331 (1984)]
38. Ivanov V V et al. *Sverkhprovodimost': Fiz. Khim. Tekhnol.* **5** (6) 1112 (1992) [*Superconductivity* **5** (6) 1108 (1992)]
39. Ivanov V V et al. *Nanostruct. Mater.* **6** (1 – 4) 287 (1995)
40. Ivanov V V, Vikhrev A N, Nozdrin A A *Fiz. Khim. Obrab. Mater.* (3) 67 (1997)
41. Andrievskii R A et al. *Fiz. Met. Metalloved.* **81** (1) 137 (1996) [*Phys. Met. Metallogr.* **81** (1) 92 (1996)]
42. Hoefler H J, Hahn H, Averback R S *Defect and Diffusion Forum* **75** (1) 99 (1991)
43. Okada S et al. *J. Alloys Comp.* **211/212** 494 (1994)
44. Bykovskii Yu A et al. *Poverkhnost* (12) 69 (1992)
45. Dudko D A et al. *Dokl. Akad. Nauk SSSR* **285** (1) 106 (1985) [*Sov. Phys. Dokl.* **30** (11) 973 (1985)]
46. Barg A E et al. *Metallofizika* **9** (4) 118 (1987)
47. Andrievskiĭ R A *Usp. Khim.* **66** (1) 57 (1997)
48. Van Swygenhoven H et al. *Nanostruct. Mater.* **6** (5 – 8) 739 (1995)
49. Hotchandani S, Kamat P V *J. Phys. Chem.* **96** (16) 6834 (1992)
50. Bedjia I, Hotchandani S, Kamat P V *J. Phys. Chem.* **97** (42) 11064 (1993); **98** (15) 4133 (1994)
51. O'Regan B, Grätzel M, Fitzmaurice D *Chem. Phys. Letters* **183** (1) 89 (1991)
52. Yoshiki H K, Fujishima A *J. Electrochem. Soc.* **142** (2) 428 (1995)
53. Kavan L et al. *J. Phys. Chem.* **97** (37) 9493 (1993)
54. Yamada K et al. *J. Non-Cryst. Solids* **100** (1 – 3) 316 (1988)
55. Lu K, Wang J T, Wei W D *Scr. Metall. Mater.* **25** (3) 619 (1991)
56. Cheng T *Nanostruct. Mater.* **2** (1) 19 (1992)
57. Hoffmann H *Thin Solid Films* **58** 223 (1979)
58. Yoshizawa Y, Oguma S, Yamauchi K *J. Appl. Phys.* **64** (10, part 2) 6044 (1988)
59. Noskova N I et al. *Fiz. Met. Metalloved.* **73** (2) 102 (1992) [*Phys. Met. Metallogr.* **73** (2) 181 (1992)]
60. Noskova N I et al. *Fiz. Met. Metalloved.* **76** (5) 171 (1993) [*Phys. Met. Metallogr.* **76** (5) 535 (1993)]
61. Inoue A et al. *Mater. Trans. Japan. Inst. Met.* **35** 85 (1994)
62. Smirnova N A et al. *Fiz. Met. Metalloved.* **62** (3) 566 (1986)
63. Valiev R Z et al. *Dokl. Akad. Nauk SSSR* **301** (4) 864 (1988) [*Sov. Phys. Dokl.* **33** (8) 626 (1988)]
64. Valiev R Z, Krasilnikov N A, Tsenev N K *Mater. Sci. Eng. A* **137** 35 (1991)
65. Valiev R Z, Korznikov A V, Mulyukov R R *Fiz. Met. Metalloved.* **73** (4) 70 (1992) [*Phys. Met. Metallogr.* **73** (4) 373 (1992)]
66. Valiev R Z, Korznikov A V, Mulyukov R R *Mater. Sci. Eng. A* **168** 141 (1993)
67. Akhmadeev N A et al. *Metally* (5) 96 (1992)
68. Rempel' A A et al. *Dokl. Ross. Akad. Nauk* **347** (6) 750 (1996) [*Phys. Dokl.* **41** (4) 152 (1996)]
69. Cziraki A et al. *Nanostruct. Mater.* **6** (5 – 8) 547 (1995)
70. Rempel' A A et al. *Metallofiz. Noveishie Tekhnol.* **18** (7) 14 (1996)
71. Rempel A A, Gusev A I *Phys. Status Solidi B* **196** (1) 251 (1996)
72. Rempel A A et al. *Nanostruct. Mater.* **7** (6) 667 (1996)
73. Rempel' A A et al. *Dokl. Ross. Akad. Nauk* **345** (3) 330 (1995) [*Phys. Dokl.* **40** (11) 570 (1995)]
74. Valiev R Z et al. *Metallofizika* **12** (5) 124 (1990)
75. Valiev R Z, Mulyukov R R, Ovchinnikov V V *Philos. Mag. Lett.* **62** (4) 253 (1990)
76. Valiev R Z et al. *Scr. Metall. Mater.* **25** (12) 2717 (1991)
77. Valiev R Z et al. *Pis'ma Zh. Tekh. Fiz.* **15** (1) 78 (1989) [*Sov. Tech. Phys. Lett.* **15** (1) 33 (1989)]
78. Valiev R Z et al. *Phys. Status Solidi A* **117** (2) 549 (1990)
79. Mulyukov Kh Ya et al. *J. Magn. Magn. Mater.* **89** (1) 207 (1990)
80. Mulyukov Kh Ya, Korznikova G F, Valiev R Z *Phys. Status Solidi A* **125** (2) 609 (1991)
81. Abdulov R Z, Valiev R Z, Krasilnikov N A *Mater. Sci. Lett.* **9** (12) 1445 (1990)
82. Galeev R M, Valiakhmetov O R, Salishchev G A *Izv. Akad. Nauk SSSR, Met.* (4) 97 (1990)
83. Valiakhmetov O R, Galeev R M, Salishchev G A *Fiz. Met. Metalloved.* **70** (10) 204 (1990)
84. Rempel' A A, Gusev A I, Mulyukov R R, in: *Solid-State Chemistry and New Materials* Vol. 2 (Ekaterinburg: Institute of Solid-State Chemistry, Ural Divisions, Russian Academy of Sciences, 1996) Vol. 1, p. 244
85. Rempel' A A, Gusev A I, Mulyukov R R, in: *Ul'tradispersnye Poroshki, Materialy i Nanostructury* (Ultradisperse Powders, Materials, and Nanostructures) (Ed. V E Red'kin) (Krasnoyarsk: Krasnoyarsk State Technical University, 1996) p. 131
86. Gleiter H *Nanostruct. Mater.* **6** (1 – 4) 3 (1995)
87. Gleiter H, in *Mechanical Properties and Deformation Behavior of Materials Having Ultrafine Microstructure* (Ed. M A Nastasi) (Dordrecht: Kluwer Academic Press, 1993) p. 3
88. Wunderlich W, Ishida Y, Maurer R *Scr. Metall.* **24** (2) 403 (1990)
89. Thomas G J, Siegel R W, Eastmen J A *Scr. Metall.* **24** (1) 201 (1990)
90. Mütschele T, Kirchheim R *Scr. Metall.* **21** (2) 135 (1987)
91. Schaefer H -E et al. *Nanostruct. Mater.* **1** (6) 523 (1992)
92. Zhu X et al. *Phys. Rev. B* **35** (17) 9085 (1987)
93. Fitzsimmons M et al. *Phys. Rev. B* **44** (6) 2452 (1991)
94. Eastmen J A et al. *Nanostruct. Mater.* **1** (1) 47 (1992)
95. Löffler J, Weissmüller J, Gleiter H *Nanostruct. Mater.* **6** (5 – 8) 567 (1995)
96. Weissmüller J, Löffler J, Kleber M *Nanostruct. Mater.* **6** (1 – 4) 105 (1995)
97. Haubold T et al. *Phys. Lett. A* **135** (8 – 9) 461 (1989)
98. Ishida Y et al. *Nanostruct. Mater.* **6** (1 – 4) 115 (1995)
99. Schlorke N et al. *Nanostruct. Mater.* **6** (5 – 8) 593 (1995)
100. Babanov Yu A et al. *Nanostruct. Mater.* **6** (5 – 8) 601 (1995)
101. Jorra E et al. *Philos. Mag. B* **60** (2) 159 (1989)
102. Sanders P et al. *Scr. Metall. Mater.* **29** (1) 91 (1993)
103. Würschum R, Greiner W, Schaefer H-E *Nanostruct. Mater.* **2** (1) 55 (1993)
104. Lapovok V N et al. *Fiz. Tverd. Tela* (Leningrad) **25** (6) 1846 (1983) [*Sov. Phys. Solid State* **25** (6) 1063 (1983)]
105. Schaefer H-E et al. *Phys. Rev. B* **38** (14) 9545 (1988)

106. Schaefer H-E et al., in *Positron Annihilation* (Eds L Dorikens-Vanpraet, M Dorikens, D Segers) (Singapore: World Scientific Publ. Comp., 1989) p.79
107. Würschum R, Scheytt M, Schaefer H -E *Phys. Status Solidi A* **102** (1) 119 (1987)
108. Schaefer H-E *Phys. Status Solidi A* **102** (1) 47 (1987)
109. Schaefer H-E et al. *Nanostruct. Mater.* **6** (5 – 8) 869 (1995)
110. Würschum R *Mater. Sci. Forum* **105 – 110** 1337 (1992)
111. Würschum R et al. *Scr. Metall. Mater.* **25** (11) 2451 (1991)
112. Puska M J, Nieminen R M *J. Phys. F: Met. Phys.* **13** (2) 333 (1983)
113. Dlubek G et al. *J. Phys. F: Met. Phys.* **9** (10) 1961 (1979)
114. Alekseeva O K et al. *Phys. Status Solidi B* **95** (2) K135 (1979)
115. Würschum R et al. *J. Phys.: Condens. Matter* **1** Suppl. A, SA33 (1989)
116. Puska M J, Corbell C *Phys. Rev. B* **38** (14) 9874 (1988)
117. Schaefer H-E, Forster M *Mater. Sci. Eng. A* **109** 161 (1989)
118. Nazarov A A, Romanov A E, Valiev R Z *Acta Metall. Mater.* **41** (4) 1033 (1993)
119. Nazarov A A, Romanov A E, Valiev R Z *Nanostruct. Mater.* **4** (1) 94 (1994)
120. Gertsman V Yu et al. *Scr. Metall. Mater.* **30** (2) 229 (1993)
121. Valiev R Z *Nanostruct. Mater.* 6 (1 – 4) 73 (1995)
122. Nazarov A A, Romanov A E, Valiev R Z *Nanostruct. Mater.* **6** (5 – 8) 775 (1995)
123. Gutkin M Yu, Ovid'ko I A, Mikaelyan K N *Nanostruct. Mater.* **6** (5 – 8) 779 (1995)
124. Gutkin M Yu, Mikaelyan K N, Ovid'ko I A *Fiz. Tverd. Tela* (St. Petersburg) **37** (2) 552 (1995) [*Phys. Solid State* **37** (2) 300 (1995)]
125. Rybin V V, Zisman A A, Zolotarevsky N Yu *Acta Metal. Mater.* **41** (9) 2211 (1993)
126. Musalimov R Sh, Valiev R Z *Scripta Metall. Mater.* **27** (12) 1685 (1992)
127. Gusev A I, Rempel' A A *Strukturnye Fazovye Perekhody v Nestekhiometrticheskikh Soedineniyakh* (Structural Phase Transitions in Nonstoichiometric Compounds) (Moscow: Nauka, 1988)
128. Bologh J et al. *Nanostruct. Mater.* **2** (1) 11 (1993)
129. Eastmen J A, Fitzsimmons M, Thompson L J *Philos. Mag. B* **66** (5) 667 (1992)
130. Qin X Y, Wu X J, Cheng L F *Nanostruct. Mater.* **2** (1) 99 (1993)
131. Sui M L, Lu K *Mater. Sci. Eng. A* **179 – 180** 541 (1994)
132. Lu K, Sui M *J. Mater. Sci. Technol.* **9** (6) 419 (1993)
133. Zhang H Y, Lu K, Hu Z Q *Nanostruct. Mater.* **6** (1 – 4) 489 (1995)
134. Cimino A, Porba P, Valigi M *J. Am. Chem. Soc.* **409** (1) 152 (1966)
135. Hellstern E et al. *J. Appl. Phys.* **65** (1) 305 (1989)
136. Neiman G W, Weertman J R, Siegel R W *J. Mater. Res.* **6** (5) 1012 (1991)
137. Aleksandrov I V, Valiev R Z *Fiz. Met. Metalloved.* **77** (6) 77 (1994) [*Phys. Met. Metallogr.* **77** (6) 623 (1994)]
138. Alexandrov I V, Valiev R Z *Philos. Mag. B* **73** (6) 861 (1996)
139. Alexandrov I V, Valiev R Z *Nanostruct. Mater.* **6** (5 – 8) 763 (1995)
140. Zhang K et al. *J. Appl. Phys.* **80** (10) 5617 (1996)
141. Valiev R Z et al. *Mater. Sci. Forum* **235 – 238** 497 (1997)
142. Hall E O *Proc. Phys. Soc. B* (London) **64** part 9 (381B) 747 (1951)
143. Petch N J *J. Iron Steel Inst.* **174** (1) 25 (1953)
144. Tabor D *The Hardness of Metals* (London: Oxford University Press, 1951)
145. Coble R L *J. Appl. Phys.* **34** (6) 1679 (1963)
146. Chokshi A H et al. *Scr. Metall.* **23** (10) 1679 (1989)
147. Lu K, Wei W D, Wang J T *Scr. Metall.* **24** (12) 2319 (1990)
148. Christman T, Jain M *Scr. Metall. Mater.* **25** (4) 767 (1991)
149. Chang H et al. *Scr. Metall. Mater.* **25** (5) 1161 (1991)
150. Kim K, Okazaki K *Mater. Sci. Forum* **88 – 90** 553 (1992)
151. Jang J S C, Koch C C *Scr. Metall.* **24** (8) 1599 (1990); **24** (10) 2023 (1990)
152. Ganapathi S K et al. *Mater. Res. Soc. Symp. Proc.* **206** 597 (1991)
153. Hughes D et al. *Scr. Metall.* **20** (1) 93 (1986)
154. Fougere G E, Weertman J R, Siegel R W *Nanostruct. Mater.* **3** (3) 379 (1993)
155. Siegel R W, Fougere G E *Nanostruct. Mater.* **6** (1 – 4) 205 (1995)
156. Hahn H, Padmanabhan K A *Nanostruct. Mater.* **6** (1 – 4) 191 (1995)
157. Valiev R Z et al. *Scr. Metall. Mater.* **27** (7) 855 (1992)
158. Kizuka T et al. *Philos. Mag. A* **69** (3) 551 (1994)
159. He L, Ma E *Nanostruct. Mater.* **7** (3) 327 (1996)
160. Haubold T, Gertsman V *Nanostruct. Mater.* **1** (4) 303 (1992)
161. Holtz R L, Provenzano V *Nanostruct. Mater.* **4** (3) 241 (1994)
162. Akhmadeev N A et al. *Fiz. Tverd. Tela* (Leningrad) **34** (10) 3155 (1992) [*Sov. Phys. Solid State* **34** (10) 1687 (1992)]
163. Korn D et al. *J. Phys. Coll. C5* **49** Suppl. (5) C5-769 (1988)
164. Lebedev A B et al. *Fiz. Tverd. Tela* (St. Petersburg) **38** (6) 1775 (1996) [*Phys. Solid State* **38** (6) 978 (1996)]
165. Mulyukov R R et al. *Mater. Sci. Eng. A* **171** 143 (1993)
166. Akhmadeev N A et al. *Acta Metall. Mater.* **41** (4) 1041 (1993)
167. Mulyukov R R et al. *Metallofizika* **15** (1) 50 (1993)
168. Mulyukov R R et al. *Mater. Sci. Forum* **170 – 172** 159 (1994)
169. Mulyukov R R et al. *Nanostruct. Mater.* **6** (5 – 8) 577 (1995)
170. Mulyukov R R et al. *Mater. Res. Bull.* **31** (6) 639 (1996)
171. Mulyukov R R et al. *Mater. Sci. Forum* **225 – 227** 787 (1996)
172. Pearson C E *J. Inst. Metals* **54** (1) 111 (1934)
173. Wakai F, Sakagushi S, Matsuno Y *Adv. Ceram. Mater.* **1** (3) 259 (1986)
174. Wakai F et al. *Nature* (London) **344** (6265) 421 (1990)
175. Sherby O D, Ruano O A, in *Superplastic Forming of Structural Alloys* (Eds N E Paton, C H Hamilton) (New York: The Metall. Soc. of AIME, 1982) p. 241
176. Wang J -G, Raj R *J. Am. Ceram. Soc.* **67** (6) 385 (1984)
177. Karch J, Birringer R, Gleiter H *Nature* (London) **330** (6148) 556 (1987)
178. Rupp J, Birringer R *Phys. Rev. B* **36** (15) 7888 (1987)
179. Tschöpe A, Birringer R *Philos. Mag. B* **68** (2) 223 (1993)
180. Stuhr U et al. *Nanostruct. Mater.* **6** (5 – 8) 555 (1995)
181. Eastmen J A, Thompson L J, Kestel B J *Phys. Rev. B* **48** (1) 84 (1993)
182. Goll G, Löhneyen H *Nanostruct. Mater.* **6** (5 – 8) 559 (1995)
183. Trampenau J et al. *Nanostruct. Mater.* **6** (5 – 8) 551 (1995)
184. Wang J et al. *Nanostruct. Mater.* **6** (5 – 8) 747 (1995)
185. Pirc R, Holz A *Nanostruct. Mater.* **6** (5 – 8) 755 (1995)
186. Zhu X PhD Thesis (Saarbrücken, Germany: University of Saarbrücken, 1986)
187. Klam H J, Hahn H, Gleiter H *Acta Metall.* **35** (8) 2101 (1987)
188. Sui M L, Lu K *Nanostruct. Mater.* **6** (5 – 8) 651 (1995)
189. Gärtner F et al. *Scr. Mater.* **35** (7) 805 (1996)
190. Tschöpe A, Birringer R, Gleiter H *J. Appl. Phys.* **71** (9) 5391 (1992)
191. Kai H Y PhD Thesis (Amsterdam: Universiteit van Amsterdam, 1993)
192. Frolov G I et al. *Fiz. Tverd. Tela* (St. Petersburg) **38** (4) 1208 (1996) [*Phys. Solid State* **38** (4) 668 (1996)]
193. Islamgaliev R K et al. *Metallofizika* **12** (2) 317 (1990)
194. Islamgaliev R K et al. *Phys. Status Solidi A* **118** (1) K27 (1990)
195. Pekala K, Pekala M *Nanostruct. Mater.* **6** (5 – 8) 819 (1995)
196. Mulyukov R R Doctoral (Phys.–Math.) Dissertation (Moscow: Moscow State Technical University — Moscow Institute of Steel and Alloys, 1997)
197. Liu K L et al. *J. Magn. Magn. Mater.* **12** (1) 43 (1979)
198. Mueller F M et al. *Phys. Rev. B* **1** (12) 4617 (1970)
199. Kriessman C J, Callen H B *Phys. Rev.* **94** (4) 837 (1954)
200. Weiss W D, Kohlhaas R *Z. Angew. Phys.* **23** (3) 175 (1967)
201. *Physical Metallurgy* (Ed. R W Cahn) (Amsterdam: North-Holland, 1965)
202. Wurschum R et al. *Ann. Chim. Sci. Mater.* **21** (5) 471 (1996)
203. Garber M, Henry W G, Hoeve H G *Can. J. Phys.* **38** (12) 1595 (1960)
204. Tammann G, Oelsen W *Z. Anorg. Chem.* **186** 257 (1930)
205. Bitter F et al. *Phys. Rev.* **60** (2) 134 (1941)
206. Vonsovskiĭ S V *Magnetism* Vol. 2 (New York: Wiley, 1971)
207. Kittel C *Introduction to Solid State Physics* (New York: Wiley, 1956)
208. Kisker H et al. *Nanostruct. Mater.* **6** (5 – 8) 925 (1995)
209. Kronmüller H *Phys. Status Solidi B* **144** (1) 385 (1987)
210. Korolev A V et al. *Fiz. Met. Metalloved.* **68** (4) 672 (1989)
211. Hahn A *Ann. Phys.* **11** (7 – 8) 277 (1963)
212. Korolev A V et al. *Fiz. Met. Metalloved.* **70** (11) 98 (1990)
213. Hirscher M et al. *J. Magn. Magn. Mater.* **146** (1) 117 (1995)
214. Yamauchi K, Yoshizawa Y *Nanostruct. Mater.* **6** (1 – 4) 247 (1995)
215. Zhalnin B V et al. *Fiz. Met. Metalloved.* **79** (5) 94 (1995) [*Phys. Met. Metallogr.* **79** (5) 536 (1995)]
216. Wang N, Zhu F, Haasen P *Philos. Mag. Lett.* **64** (3) 157 (1991)
217. Noskova N I et al. *Fiz. Met. Metalloved.* **74** (1) 80 (1992) [*Phys. Met. Metallogr.* **74** (1) 52 (1992)]

218. Glazer A A, et al. *Fiz. Met. Metalloved.* **74** (2) 96 (1992) [*Phys. Met. Metallogr.* **74** (2) 163 (1992)]
219. Hono K et al. *Acta Metall. Mater.* **40** (9) 2137 (1992)
220. Sosnin V V et al. *Fiz. Met. Metalloved.* **78** (2) 140 (1994) [*Phys. Met. Metallogr.* **78** (2) 218 (1994)]
221. Noskova N I et al. *Fiz. Met. Metalloved.* **76** (5) 171 (1993) [*Phys. Met. Metallogr.* **76** (5) 535 (1993)]
222. Baricco M et al. *Mater. Sci. Eng. A* **179 – 180** 572 (1994)
223. Clavaguera N et al. *Nanostruct. Mater.* **6** (1 – 4) 453 (1995)
224. Conde C F, Conde A *Nanostruct. Mater.* **6** (1 – 4) 457 (1995)
225. Surinach S et al. *Nanostruct. Mater.* **6** (1 – 4) 461 (1995)
226. Graf T et al. *Nanostruct. Mater.* **6** (1 – 4) 469 (1995)
227. Noskova N I. Ponomareva E G *Fiz. Met. Metalloved.* **82** (5) 163 (1996) [*Phys. Met. Metallogr.* **82** (5) 542 (1996)]
228. Hasegawa N, Saito M *J. Magn. Soc. Japan.* **14** (2) 313 (1990)
229. Taneko N et al. *Jpn. J. Appl. Phys.* **30** (2A) L195 (1991)
230. Inoue A *Nanostruct. Mater.* **6** (1 – 4) 53 (1995)
231. Noskova N I et al. *Fiz. Met. Metalloved.* **73** (2) 102 (1992) [*Phys. Met. Metallogr.* **73** (2) 181 (1992)]
232. Glazer A A et al. *Fiz. Met. Metalloved.* **76** (2) 171 (1993) [*Phys. Met. Metallogr.* **76** (2) 222 (1993)]
233. Noskova N I et al. *Nanostruct. Mater.* **6** (5 – 8) 969 (1995)
234. Lyakishev N P *Vestnik Ross. Akad. Nauk* **67** (5) 403 (1997)